IEEE Access
Multidisciplinary | Rapid Review | Open Access Journal

Received November 2, 2021, accepted December 2, 2021, date of publication December 6, 2021,
date of current version December 20, 2021.

Digital Object Identifier 10.1109/ACCESS.2021.3132963

Flight Test of L_1 Adaptive Control on 120-kg-Class Electric Vertical Take-Off and Landing Vehicles

ZIAN WANG[1], ZHENG GONG[1], CHI ZHANG[2], JUN HE[3], AND SHENGCHEN MAO[1]
[1]School of Aerospace Engineering, Nanjing University of Aeronautics and Astronautics, Nanjing 210016, China
[2]COMAC Beijing Aircraft Technology Research Institute, Beijing 100083, China
[3]School of Aerospace Engineering, Shenyang Aerospace University, Shenyang 110000, China

Corresponding author: Zheng Gong (matthewzhenggong@nuaa.edu.cn)

This work was supported by the National Natural Science Foundation of China under Grant 11402115.

ABSTRACT Electric vertical take-off and landing vehicles (eVTOLs) are a novel class of transportation that can facilitate point-to-point travel. However, the control of eVTOLs traversing from the gyro to the fixed-wing flight mode poses daunting challenges in the context of modeling, the design of the control algorithm, flight management, simulation, verification, and testing. This paper proposes the design of an $\mathcal{L}_1$-augmented autopilot that is implemented on the 120-kg-class large-scale Electric Transportation 120 platform of the Commercial Aircraft Corporation of China, Ltd. Significant advances in fast rotor modeling according to blade element momentum theory, virtual flight test techniques in wind tunnels, a layered design of the architecture for flight management, and fast techniques for validation and verification speed-up the development of the flight control system (FCS). The state-of-the-art $\mathcal{L}_1$ adaptive control architecture combined with dynamic inversion type control allocator is particularly suitable for dealing with nonaffine control problems encountered with aerodynamic uncertainties. Implement of $\mathcal{L}_1$ adaptive control theory significantly reduces the parameter tuning cycle to achieve the desired closed-loop tracking performance. Real-word flight tests have confirmed the effectiveness of $\mathcal{L}_1$-augmented algorithm and customized FCS.

INDEX TERMS Blade element momentum theory, electric vertical take-off and landing vehicle, flight control system, flight test, $\mathcal{L}_1$ adaptive control, virtual flight test.

I. INTRODUCTION

Electric Vertical Takeoff and Landing vehicle (eVTOL) is a novel class of transportation based on the concept of Urban Air Mobility (UAM). With the virtues of being low cost, on demand, point to point and environment-friendly, eVTOLs have promising application prospects in intra-city passenger air services [1]–[4]. The high-cost and large-scale Electric Transportation 120 (ET120) vehicle shown in FIGURE 1 is a hybrid-wing configuration being explored by the Commercial Aircraft Corporation of China Ltd (COMAC), equipped with a distributed vertical and forward electric propulsion system. This propulsion system highlights four pairs of vertically mounted rotors, of which the upper and lower rotors works in pairs coaxially and direction-contrarily to provide hovering power, and one separated horizontally mounted rotor to provide fixed-wing propulsion power. The propulsion system, which can switch between gyro mode and fixed-wing mode, are powered by lithium polymer batteries with high-voltage brushless direct-current motors. Qualified with the convenience of VTOL capability and the efficiency of the fixed-wing high lift-to-drag ratio level-flight performance, the ET120 achieves the design purpose of reducing traffic jams during peak hours and urban commuting time. In January 2021, the ET120 has been successfully tested at the Jian general airport, Jiangxi, China. Such a configuration reflects the development direction of UAM vehicles.

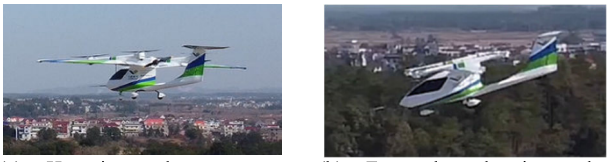

(a) Hovering mode. (b) Forward-acceleration mode.

FIGURE 1. The flight test of an ET120 vehicle at the Jian general airport, Jiangxi, China.

New configurations and multiple flight modules require the corresponding flight management architecture, controller,

The associate editor coordinating the review of this manuscript and approving it for publication was Rosario Pecora.

criterion for control allocation, and flight control system (FCS) capable of automatically stabilizing and guiding the vehicle in the hovering, loitering and cruising flight modes as well as accelerate/decelerate transition flight [5]. Three main challenges present: 1) the dynamics of the accelerate and decelerate transition processes are fast time-varying. The multi-rotor downwash introduces involuted aerodynamic forces and moments on wing body that affect the trim characteristics [6]. The cross-coupling between wing-body and rotors also poses difficulties in aerodynamic modeling and control designing; 2) it is a typical multi-input system that both aerodynamic forces and multi-rotor thrust directly affect attitude and position motions; 3) it is also a typical underactuated platform, which requires specific control inputs to control position movements via attitude changes in different flight modes.

Research on flight control schemes for such new configurations has long been ongoing. First, the design of classical proportional-integral-derivative control in the form of gain scheduling is limited in terms of stability and robustness, and requires long iteration cycles [6]. Second, such computational controllers as the artificial neural network [7] and model predictive control [8] can be used to implement stable control, but practical applications of computational algorithms are hampered by its requirement of high-performance computing resources to execute large-scale numerical calculations within a limited lead period. Third, other control theories, such as nonlinear dynamic inversion (NDI) [9] and quantitative feedback theory [10], are model-based, and are sensitive to time-varying dynamics and unmatched uncertainties. In the context of the fight characteristics of ET120, the development of an adaptive theory to enhance the robustness and flight quality is important.

The $\mathcal{L}_1$ adaptive control algorithm is a fast and robust adaptive control law that decouples adaptation from robustness by using a low-pass filter and has become increasingly popular among the modern high-performance aircraft designers [11], [12]. The tracking performance of $\mathcal{L}_1$ adaptive enhanced technology has been shown to be satisfactory in multiple successful flight tests [13]. It is sufficiently fast to be applied to a time-varying system, and to allow for the compensation of the undesirable effects of rapidly varying uncertainties and significant changes in system dynamics [15]. In addition, the adaptive law reduces oscillations in control, thus guaranteeing dynamic performance and robustness [14]. Thus, the $\mathcal{L}_1$ adaptive control architecture is a feasible method to solve the problems caused by inaccurate modeling. Compared with conventional control algorithms where the process of parameters tuning is time consuming, the adaptive gains of $\mathcal{L}_1$ adaptive control can be easily tuned by selecting the appropriate bandwidth according to military flight quality (e.g., MIL-STD-1797B) [16]. Furthermore, the tracking performance can be guaranteed consistency in the entire flight envelope with fixed gains, effectively avoiding gain-scheduling [12].

Motivated by the above discussion, this study proposes a model and the customized FCS to address the above problems. First, to consider the influence of oblique inflow, a fast rotor dynamics model is established based on blade element momentum theory (BEMT). Second, to handle the strong aerodynamic cross-coupling caused by the wing body and the multi-rotors, an $\mathcal{L}_1$ adaptive controller is used to eliminate and compensate for the disturbance and unmatched uncertainties. Third, to test and verify multiple flight modes sequentially, a hierarchical flight management architecture is designed. The design of the configuration platform and control scheme are both tested and verified through virtual and empirical flight tests. The virtual flight test is usually carried out in a wind tunnel before the actual flight test in preliminary design phases, and is used for risk assessment and safety enhancement [17], [18]. This is followed by practical flight tests to evaluate the feasibility and capability of the platform [19]–[22]. The main contributions of this work are as follows:

1. The nonlinear model developed for simulation.
2. The corresponding single-input-single-output (SISO) $\mathcal{L}_1$ adaptive augmentation algorithm, hierarchical flight management architecture, multi-modal control logic, and control allocator are designed.
3. Validation of the algorithms in virtual flight test in wind tunnel and actual flight test results performed on the ET120.

II. MODELING FOR SIMULATION

A six-degree-of-freedom (six-DOF) flight dynamics model is required to describe the states of ET120, and contains two main parts: the aerodynamics part and the power system part. The aerodynamics part is concerned with the clean fixed-wing aerodynamics acting on the vehicle. The power system part calculates the forces and moments provided by the power system of rotors, including eight hovering rotors and an auto-throttle rotor. The six-DOF flight dynamics model was built by considering three issues: 1) evaluation of flight characteristics and performance, 2) linearization of trim points for control design, and 3) facilitating Monte Carlo numerical simulations. The simulation environments in this work were built in MATLAB/SIMULINK. High-quality aerodynamic data were obtained from wind tunnel tests. The forces and moments of the propulsion part were acquired by BEMT.

A. SYSTEM INTRODUCTION

1) PLATFORM DESIGN

The ET120 is a composite platform featuring multiple rotors and a fixed wing. The advantages of the layout of the platform are as follows: 1) The center of the resultant lift provided by the hovering power system is at the center of gravity (CG) of the ET120, thus no rotor power wasted on trimming the additional pitching moments. 2) The redundant rotor system renders the vehicle controllable even if one rotor fails.

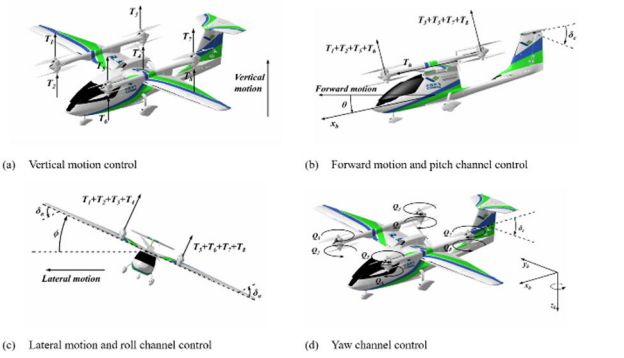

FIGURE 2. The mechanical configuration and control principles of ET120.

3) The energy used is electric, and thus green, environmentally friendly, and reusable. 4) The layout of the wing and the power system of the rotor allow for quick mounting and unmounting. 5) The layout of the high T tail reduces the effect of the rotor on the elevator.

The ET120 power system is divided into a hovering and a propulsion power system. The propulsion power system consists of only one rotor that is mounted horizontally behind the cabin to provide fixed wing-mode power. The hovering system contains eight rotors divided into four pairs. Each pair contains an upper and a lower rotor that are mounted coaxially and vertically on the body of the wing. The configuration of the power system makes ET120 an under-actuated platform in which positional motion can be controlled via attitude motion. Vertical motion is controlled by the total speed of the hovering rotors n_v at hover or low-speed conditions and elevator δ_v in fixed-wing flight, as shown in FIGURE 2 (a). Longitudinal forward motion is driven by the tilting pitch attitude in multi-rotor mode and the propulsion power in fixed-wing flight. In the attitude-driven mode, the forward and backward accelerations are produced by tilting the pitch attitude to provide the longitudinal projection of the hovering rotor thrust. Correspondingly, the pitch control principle is to control the deflection of elevator δ_e and the differential speeds of the four hovering rotors at the front and back, n_θ, as shown in FIGURE 2(b). The lateral motion is driven by tilting bank attitude both in multi-rotor and fixed-wing modes. Correspondingly, the roll control principle is used to control the aileron δ_a, and the differential speeds of the four left and right rotors, n_ϕ, as shown in FIGURE 2(c). The yaw channel control relied on the control of the rudder δ_r and the differential speeds of the clockwise and anticlockwise rotors, n_ϕ, as shown in FIGURE 2(d). FIGURE 2 shows the control principles of the configuration.

If the virtual input vector is $\boldsymbol{U} = [n_v, n_\phi, n_\theta, n_\varphi, n_9, \delta_e, \delta_a, \delta_r]^T$, the actual input vector is $\boldsymbol{U}_a = [n_1^c, n_2^a, n_3^a, n_4^c, n_5^a, n_6^c, n_7^c, n_8^a, n_9, \delta_e, \delta_a, \delta_r]^T$,where n_k^* represents the speed of each hovering rotor, $(k = 1, 2 \ldots, 8)$ represents the serial number of the rotors(consistent with the forces and torques labeled in FIGURE 2(d), $* \in \{c, a\}$ represents the direction of rotor rotation, 'c' is clockwise and 'a' is anticlockwise (consistent

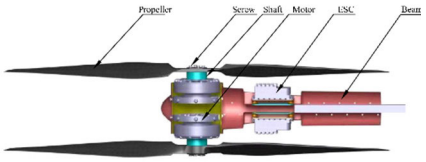

FIGURE 3. The mechanism of the hovering rotors.

with the torques defined in FIGURE 2(d)), and n_9 is the speed of the propulsion rotor, the relation between the actual input and the virtual input can be expressed as:

$$\boldsymbol{U}_a = \mathbf{R}\boldsymbol{U} \tag{1}$$

where $\mathbf{R}$ is a mixed matrix:

$$\begin{aligned}
\mathbf{R} &= \begin{bmatrix} \mathbf{R}_1 & & \\ & \mathrm{R}_2 & \\ & & \mathbf{R}_3 \end{bmatrix}, \\
\mathbf{R}_1 &= \begin{bmatrix} 1 & -1 & 1 & 1 \\ 1 & -1 & 1 & -1 \\ 1 & -1 & -1 & 1 \\ 1 & -1 & -1 & -1 \\ 1 & 1 & 1 & -1 \\ 1 & 1 & 1 & 1 \\ 1 & 1 & -1 & -1 \\ 1 & 1 & -1 & 1 \end{bmatrix}, \\
R_2 &= [1], \\
\mathbf{R}_3 &= \begin{bmatrix} 1 & & \\ & 1 & \\ & & 1 \end{bmatrix}
\end{aligned} \tag{2}$$

where $\mathbf{R}$ is an 11×8 matrix, $\mathbf{R}_1$ is an 8×4 matrix represents the relationships between the actual inputs $n_k^*(k = 1, 2 \ldots, 8)$ and the virtual inputs $n_v, n_\phi, n_\theta, n_\varphi$. Noticed that n_k^* are all scalar quantities with a positive value, but the rotor direction impacts the rotor torques (plus or minus), the impact of the rotor direction is presented in $\mathbf{R}_1$ by the plus or minus characteristics of the elements in its 4-th column. R_2 and $\mathbf{R}_3$ are unit matrixes of 1×1 and 3×3 dimensions, for that the virtual inputs and the actual inputs corresponding to them, $n_9, \delta_e, \delta_a, \delta_r$, are the same.

2) MECHANICAL DESIGN

The mechanism of the hovering rotors and the propulsion rotor are all the same. As shown in FIGURE 3, the hovering rotor system is composed by a propeller, a motor, and an electronic speed controller (ESC). The propeller is linked directly to the end face of the motor shaft by four screws. The motors are inserted in a sleeve at the end of the beam. The ESC is mounted near the motors on the beam to shorten the length of the wire connecting it to the motor. As shown in FIGURE 4, the mechanism design of the propulsion rotor system is similar to that of the hovering rotor system. The difference exists in two aspects: 1. The propulsion rotor is mounted horizontally behind the tail-wing of the ET120; 2. The rotor is connected to the motor directly with a cowling to

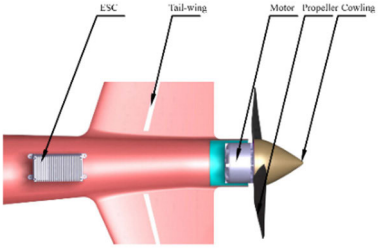

FIGURE 4. The mechanism of the propulsion rotor.

FIGURE 5. A 16.67% scale tunnel model of ET120 in a low-speed wind tunnel.

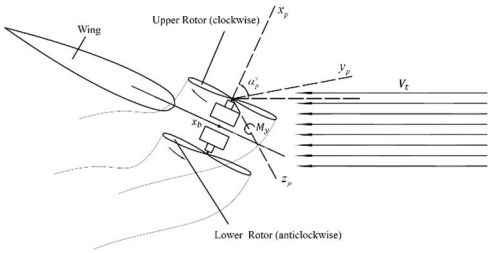

FIGURE 6. Diagram of oblique inflow to the fore-left rotors in the transition flight.

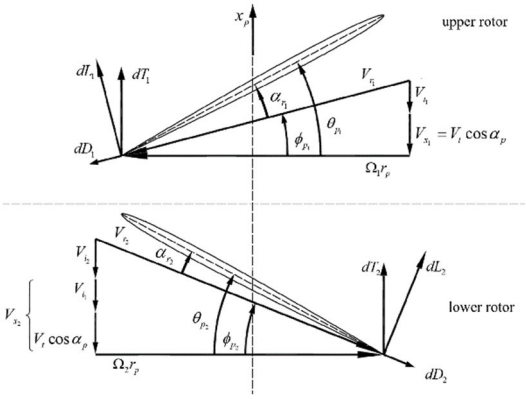

FIGURE 7. The blade profile of a pair of hovering rotors.

decrease the forward flight drag. Since all the propellers are linked directly by either screws or cowling, this feature leads to an absence of the cyclic pitch control of the rotors. So, the controlled variables of the rotor system are only the rotating speeds. Also, this feature causes the inability of a single propeller to self-balance the overturning moments caused by the oblique in flow, this will influence the longitudinal trimming characteristics of the ET120 significantly.

B. THE AERODYNAMIC MODEL

The layout of ET120 inevitably generates aerodynamic coupling between the multi-rotor power system and the wing body in the transition phase. To assess the flight characteristics and performance, only the high-quality and clean aerodynamic data that are acquired by implementing wind tunnel experiments, as shown in FIGURE 5. The additional aerodynamic forces and moments acting on the wing body caused by the multi-rotor power system can be constructed by using the approach in Ref [23].

The forces and moments acting on the aircraft are:

$$\begin{cases} L = L\left(V_t, \alpha, q, \delta_e\right) \\ D = D\left(V_t, \alpha, q, \delta_e\right) \\ S = S\left(V_t, \beta, p, r, \delta_r\right) \\ l_a = l_a\left(V_t, \beta, p, r, \delta_a, \delta_r\right) \\ m_a = m_a\left(V_t, \alpha, q, \delta_e\right) \\ n_a = n_a\left(V_t, \beta, p, r, \delta_a, \delta_r\right) \end{cases} \tag{3}$$

where L, D and S represent the lift, drag, and side forces of the fixed wing, respectively; l_a, m_a and n_a represent the roll, pitch, and yaw aerodynamic moments of the fixed wing, respectively; V_t represents airspeed, α and β are the angle of attack and angle of sideslip, respectively, and p, q and r are the angular rates of the roll, pitch, and yaw in the body coordinate system, respectively.

C. MODEL OF ROTOR POWER SYSTEM

1) THE HOVERING ROTOR SYSTEM

To model the hovering power system, two issues should be considered. First, the structure of the coaxial double rotors of the hovering power system leads to aerodynamic interaction between the upper and lower rotors. Second, as shown in FIGURE 6, owing to the non-negligible angle of incidence between oblique inflow and the rotor disk in the forward flight phase, an additional overturning moment is generated. As aforementioned, this moment influences the longitudinal characteristics significantly. To address the asymmetric aerodynamic loads and the influence of airflow between the upper and lower rotors, BEMT is introduced to the modeling of hovering rotor dynamics.

In BEMT, the rotor blade is discretized into a finite number of blade profiles, where momentum theory is utilized to calculate the differential thrust and torque. The blade profiles of a pair of hovering rotors are shown in FIGURE 7. The following assumptions are proposed:

Assumption 1: The upper rotor can be calculated in a typical environment of BEMT independently, because the influence of the lower rotor hardly impacts the upper rotor.

Assumption 2: The axial induced velocity of the upper profile, which impacts the lower profile, will not deviate from the axial direction, because the gap between the upper and lower profiles is narrow.

Shaping like an airfoil, the blade profile generates differential lift dL_k and drag dD_k, with a relative airspeed V_{r_k} and angle of attack α_{r_k}:

$$dL_k = C_{L_k}\frac{1}{2}\rho V_{r_k}^2 c_p dr_p \tag{4}$$

$$dD_k = C_{D_k}\frac{1}{2}\rho V_{r_k}^2 c_p dr_p \tag{5}$$

where C_{L_k}, C_{D_k} are the lift and drag coefficients relative to α_k, ρ represents the density of air, c_p is the chord length of the blade profile. The relative airspeed includes axial and circumferential components: the axial, induced velocity V_{i_k} and inflow velocity V_{x_k}; the circumferential, the rotation speed $\Omega_k r_p$.

By projecting dL_k and dD_k to the rotor frame, the differential thrust and torque can be expressed as:

$$dT_k = dL_k \cos\phi_{p_k} - dD_k \sin\phi_{p_k} \tag{6}$$

$$dQ_k = r_p(dL_k \sin\phi_{p_k} + dD_k \cos\phi_{p_k}) \tag{7}$$

where $\phi_{p_k} = \arctan((V_{i_k} + V_{x_k})/\Omega_k r_p)$ is the inflow angle of the blade profile, $\Omega_k = 2\pi \cdot n_k/60$ is the angular rate of the rotor, r_p is the radial position of the blade profile, V_{x_k} is the axial inflow velocity, for the upper profile, according to assumption 1, V_{x_k} is the axial components of the airspeed V_t; for the lower profile, according to assumption 2, V_{x_k} is the axial components of the airspeed together with the induced velocity of the upper profile, i.e.

$$V_{x_k} = \begin{cases} V_t \cos\alpha_{p_k}, & k = 1, 3, 5, 7 \\ V_t \cos\alpha_{p_k} + V_{i_{k-1}}, & k = 2, 4, 6, 8 \end{cases} \tag{8}$$

where $\alpha_{p_k} = \pi/2 - \alpha$ is the angle between the rotor x-axis and the airspeed V_t, as shown in FIGURE 6.

Substituting Eq. (4) and (5) to Eq. (8) and using $\phi_{p_k} = \arctan((V_{i_k} + V_{x_k})/\Omega_k r_p)$ to eliminate V_{i_k}, the differential thrust dT_k can be expressed as:

$$dT_k = \frac{1}{2}\rho\frac{\Omega_k^2 r_p^2}{\cos\phi_{p_k}} c_p(C_{L_p} - C_{D_p}\tan\phi_{p_k})dr_p \tag{9}$$

By applying momentum theory over an annulus of the rotor disk, dT_k can also be expressed as:

$$dT_k = 4\pi\rho r V_{i_k}(V_{x_k} + V_{i_k}) \tag{10}$$

Combining Eq. (6) and (8), the following equation is acquired:

$$C_{L_p} - C_{D_p}\tan\phi_{p_k} = \frac{8\pi\sin\phi_{p_k}}{\Omega_1 N c}(\Omega_k r_p \tan\phi_{p_k} - V_{x_k}) \tag{11}$$

By solving Eq. (11), the inflow angle ϕ_{p_k} and the induced velocity V_{i_k} can be acquired. When the inflow is absolute axial, the induced velocity is affinely distributed in circumferential direction and the overall thrust generated by the rotor can be obtained by integrating Eq. (9) throughout the radial direction.

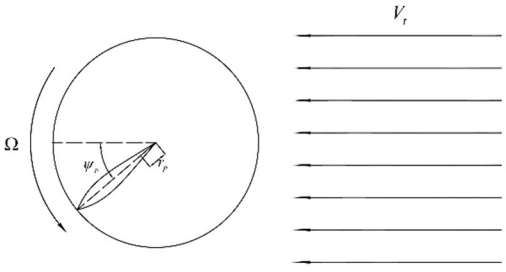

FIGURE 8. Definition of blade azimuth.

2) FORWARD FLIGHT MODEL OF HOVERING SYSTEM

The oblique flow, which is nonnegligible in forward fight phase, causes a nonaffine distribution of the induced velocity in circumferential direction, thus impacting the rotor dynamics in two aspects: 1) the differential thrusts and torques, which is concerned with the inflow angle, require corrections. 2) an overturning moment appears, deriving from the unbalanced moment of uneven thrusts, which impacts the flight trim condition of the ET120 significantly. To model these impacts, the nonaffine distributed velocity field is firstly acquired, which will then be converted to the nonaffine distributed inflow angle to correct the differential thrusts and torques. Then, the corrected differential thrusts are used to calculate the differential moments around the rotor y-axis. All these differential quantities are integrated respectively to get the thrust, torque and overturning moment of each hovering rotor.

To begin with the modeling, a new assumption is introduced:

Assumption 3: The forward flight airspeed impacts little on the blade element environment in the computational domain, for that in the computational domain, the rotor speed is quite large and the beginning computational radial position of the blade element is not near the rotation axis, thus the forward flight airspeed is small enough to be ignored compared to the rotor linear speed $\Omega_k r_p$ in circumferential direction.

According to Assumption 3, The BEMT formula derived in the hovering mode is still appropriate to forward flight mode, because the blade element environment concerns about the axial and circumferential direction only. The axial impacts of the forward flight airspeed have already been considered in BEMT by the axial inflow velocity, and the circumferential impacts can be ignored. The radial impacts are a nonaffine distribution of blade element environments throughout the rotor disk, this will be discussed in the following few paragraphs.

The nonaffine distribution of the induced velocity is related to the blade profile position, namely, the blade radial direction position r_p and the azimuth angle of the blade ψ_p (azimuth

zero is at the back line of the rotor), Thus $V_{i_k} = V_{i_k}(r_p, \psi_p)$, as shown in FIGURE 8. According to the method mentioned in Ref [23], the nonaffine induced velocity field $V_{i_k}(r_p, \psi_p)$ can be given as:

$$V_{i_k}(r_p, \psi_p) = V_{i_k 0}\left(1 + \tan\frac{\chi_k}{2} r_p \cos\psi_p\right) \tag{12}$$

where $\chi_k = \arctan(\mu_k/\lambda_k)$ represents the oblique angle of the wake of the rotor disk, $\mu_k = V_t \sin\alpha_{p_k}/\Omega_k R$ is the advance ratio of the rotor(V_t is the forward flight airspeed) and $\lambda_k = \left(V_{i_k 0} + V_{x_k}\right)/\Omega_k R$ is its inflow ratio. R is the radius of the rotor, $V_{i_k 0}$ is the average induced velocity which can be acquired by the iterative function:

$$\lambda_{k_{m+1}} = \mu \sec\alpha_{p_k} + \frac{C_T}{2\sqrt{\mu_k^2 + \lambda_{k_m}^2}} \tag{13}$$

where m is the serial number of the steps of the iteration, and C_T is thrust coefficient when the inflow is absolute axial. The initial value of λ_k can be chosen as $\lambda_{k_0} = \sqrt{\frac{C_T}{2}}$. If the iteration error satisfies $\left\|\left(\lambda_{k_{m+1}} - \lambda_{k_m}\right)/\lambda_{k_m}\right\| < \varepsilon$,($\varepsilon$ is a small quantity), the iterations stop, and λ_{k_m} is used to calculate the average induced velocity $V_{i_k 0}$; otherwise, we use the function

$$f(\lambda_k) = \lambda_k - \mu \sec\alpha_{p_k} - \frac{C_T}{2\sqrt{\mu_k^2 + \lambda_k^2}} \tag{14}$$

to update the inflow ratio λ_k as

$$\lambda_{k_{m+1}} = \lambda_{k_m} - f(\lambda_{k_m})/f'(\lambda_{k_m}) \tag{15}$$

until the cut-off condition is satisfied.

Then, the inflow angle can be organized as:

$$\phi_{p_k\psi_{p_i}}^{V_t} = \arctan\left(\frac{V_{i_k}(r_p, \psi_p) + V_{x_k}}{\Omega_k r_p}\right) \tag{16}$$

By replacing the inflow angle ϕ_{p_k} in Eq. (9) with $\phi_{p_k\psi_{p_i}}$,the corrected differential thrust and torque can be organized as:

$$dT_k = \frac{1}{2}\rho \frac{\Omega_k^2 r_p^2}{\cos\phi_{p_k\psi_{p_i}}^{V_t}} c_p (C_{L_p} - C_{D_p}\tan\phi_{p_k\psi_{p_i}}^{V_t}) dr_p \tag{17}$$

The corrected differential torque can be expressed as:

$$dQ_k = \frac{1}{2}\rho \frac{\Omega_k^2 r_p^3}{\cos\phi_{p_k\psi_{p_i}}^{V_t}} c_p (C_{D_p} + C_{L_p}\tan\phi_{p_k\psi_{p_i}}^{V_t}) dr_p \tag{18}$$

The differential moment around the rotor y-axis can be written as:

$$dM_{y_k} = \frac{1}{2}\rho \frac{\Omega_k^2 r_p^3}{\cos\phi_{p_k\psi_{p_i}}^{V_t}} \cos\psi_i c_p (C_{L_p} - C_{D_p}\tan\phi_{p_k\psi_{p_i}}^{V_t}) dr_p \tag{19}$$

With Eqs. (17), (18) and (19), the thrust, torque and overturning moment generated by each rotor can be given as: (20), shown at the bottom of the next page.

where N represents the number of blades of each rotor, m_n represents the number of azimuth angles of the blade, R_h represents the starting position of blade profiles along the radial direction, Δr_p is the differential radial length.

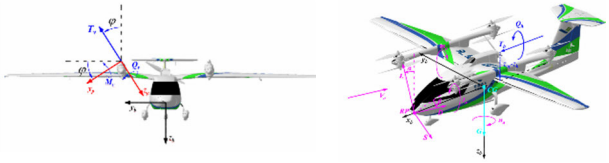

(a)Definition of camber angle

(b)The analysis of force on the ET120 vehicle.

FIGURE 9. Force analysis of ET120.

3) THE PROPULSION POWER SYSTEM

The propulsion power system contains only one propulsion rotor. In forward flight phase, the slipstream, which impacts the thrust and torque characteristics, should be considered. In this paper, the influence of slipstream is evaluated by corrected factors f_T and f_Q for C_{T_9} and C_{Q_9}. Both the corrected factors and coefficients are obtained from tests. The thrust and torque provided by the propulsion rotor can be given as:

$$\begin{cases} T_9 = f_T C_{T_9} \dfrac{1}{2}\rho\pi R^4 \Omega_9^2 \\ Q_9 = f_Q C_{Q_9} \dfrac{1}{2}\rho\pi R^5 \Omega_9^2 \end{cases} \tag{21}$$

4) NONLINEAR MODEL

In the aerodynamics and power system modeling, the forces and moments were analyzed in different frames. Usually, these variables are projected into the body frame to obtain the six dimensions of freedom (DOF) function of the vehicle. The aerodynamic forces L, D and S that are constructed in the wind frame can be projected to the body frame by a rotation matrix from the wind frame to the body frame. As a fixed camber angle, as shown in FIGURE 9 (a), is set between the axis of the rotor and the body for each hovering rotor to enhance the stability of the vehicle, the thrust, torque, and overturning moment of the hovering rotors are projected into the body frame by rotating the camber angle. The thrust and torque of the propulsion rotor can be projected to the x-axis of the body directly, for that the propulsion rotor is mounted parallel to the x-axis of the body.

The forces acting on ET120 in the x, y and z axes of the body frame F_x, F_y and F_z, respectively, can be organized as:

$$\begin{cases} F_x = -D\cos\alpha\cos\beta - S\cos\alpha\sin\beta \\ \quad + L\sin\alpha - G\sin\theta + T_9 \\ F_y = -D\sin\beta + S\cos\beta \\ \quad + G\sin\phi\cos\theta + \sum_{k=1}^{8} T_k \sin\varphi_k \\ F_z = -D\sin\alpha\cos\beta - \sin\alpha\sin\beta \\ \quad - L\cos\alpha + G\cos\phi\cos\theta \\ \quad - \sum_{k=1}^{8} T_k \cos\varphi_k \end{cases} \tag{22}$$

where φ_k is the k-th camber angle between the axis of the rotor and the x-axis of the body frame, α, β are the angle of attack and the angle of sideslip of the ET120.

As shown in FIGURE 9(b), the position of the aerodynamic reference point and the thrust line of the propulsion rotor do not coincide with the CG. This in turn causes additional moments which can be given as:

$$\begin{cases} m_{cg} = (L\cos\alpha + Y\sin\alpha\sin\beta + D\sin\alpha)(x_r - x_{cg}) \\ \quad -T_9(z_9 - z_{cg}) \\ n_{cg} = (Y\cos\beta - D\sin\beta)(x_r - x_{cg}) \end{cases} \tag{23}$$

where x_r, y_r, z_r and x_{cg}, y_{cg}, z_{cg} represent the aerodynamic reference point and the CG in body frame, respectively.

The overall moments acting on ET120 can be constructed as:

$$\begin{cases} l = l_a - \sum_{k=1}^{8} T_k \sin\varphi_k (z_k - z_{cg}) \\ \quad - \sum_{i=1}^{8} T_k \cos\varphi_k (y_k - y_{cg}) \\ \quad + Q_9 \\ m = m_a + m_{cg} \\ \quad + \sum_{k=1}^{8} T_k \cos\varphi_k (x_k - x_{cg}) \\ \quad + \sum_{k=1}^{8} M_{y_k} \cos\varphi_k - \sum_{k=1}^{8} Q_k \sin\varphi_k \\ n = n_a + n_{cg} \\ \quad + \sum_{k=1}^{8} T_k \sin\varphi_k (x_k - x_{cg}) \\ \quad + \sum_{k=1}^{8} Q_k \cos\varphi_k + \sum_{i=1}^{8} M_{y_k} \sin\varphi_k \end{cases} \tag{24}$$

where x_k, y_k, z_k are the coordinates of the k-th rotor in the body frame.

The six-DOF of the ET120 include the translation and the rotation functions, and can be expressed as:

$$\begin{cases} \dot{u} = vr - wq + F_x/m_g \\ \dot{v} = wp - ur + F_y/m_g \\ \dot{w} = uq - vp + F_z/m_g \\ l = I_x\dot{p} + (I_z - I_y)qr - I_{zx}(pq + \dot{r}) \\ m = I_x\dot{q} + (I_x - I_z)rp + I_{zx}(p^2 - r^2) \\ n = I_x\dot{r} + (I_y - I_x)pq + I_{zx}(qr - \dot{p}) \end{cases} \tag{25}$$

The kinematical function of the ET120 can be written as

$$\begin{cases} \dot{x}_g = u\cos\theta\cos\psi \\ \quad + v(\sin\theta\sin\phi\cos\psi - \cos\phi\sin\psi) \\ \quad + w(\sin\theta\cos\phi\cos\psi + \sin\phi\sin\psi) \\ \dot{y}_g = u\cos\theta\sin\psi \\ \quad + v(\sin\theta\sin\phi\sin\psi + \cos\phi\cos\psi) \\ \quad + w(\sin\theta\cos\phi\sin\psi - \sin\phi\cos\psi) \\ \dot{h} = u\sin\theta - v\sin\phi\cos\theta - w\cos\phi\sin\theta \\ \dot{\phi} = p + \tan\theta(q\sin\phi + r\cos\phi) \\ \dot{\theta} = q\cos\phi - r\sin\phi \\ \dot{\psi} = (q\sin\phi + r\cos\phi)/\cos\theta \end{cases} \tag{26}$$

where u, v and w are the velocities in the body frame; x_g, y_g, and h are positions in the inertial frame; ϕ, θ and ψ are the roll, pitch, and yaw angle, respectively; m_g represents mass;I_x, I_y and I_z are inertial moments; and I_{xy}, I_{yz} and I_{zx} are inertial products.

III. CONTROL SYSTEM DESIGN

The complete flight control scheme for the ET120 is divided into four layers: a trajectory generator, a flight management unit, a guidance layer, and a control stability augmentation layer. The trajectory generator generates navigation information relying on a trajectory planner. The main functions of the flight management unit are navigation management, waypoint management, and execution of control strategies of various flight modes, including the gyro, transition, and fixed-wing modes. The guidance layer guides the ET120 to follow a reference trajectory while maintaining the desired velocity. Because the ET120 has multiple flight modes, the guidance loop can be divided into the gyro mode and the fixed-wing mode. The control stability augmentation layer is used to enhance control stability in both rotor and fixed-wing modes. By utilizing the single-input-single-output (SISO) structure, the guidance and control algorithms in the longitudinal, lateral, and directional channels are designed independently. The complete ET120 autonomous flight control scheme is depicted in FIGURE 10. To focus on the main argument, we omit the discussion of the guidance law and detail the design of the inner loop control law.

$$\begin{cases} T_k = \frac{1}{2m_n}\rho N\Omega_k^2 \sum_{i=1}^{m_n}\sum_{r_p=R_h}^{R} \frac{r_p^2}{\cos\phi_{p_k\psi_{p_i}}^{V_t}} c_p \left(C_{L_p} - C_{D_p}\tan\phi_{p_k\psi_{p_i}}^{V_t}\right)\Delta r_p, \quad k = 1, 2\ldots, 8 \\ Q_k = \frac{1}{2m_n}\rho N\Omega_k^2 \sum_{i=1}^{m_n}\sum_{r_p=R_h}^{R} \frac{r_p^3}{\cos\phi_{p_k\psi_{p_i}}^{V_t}} c_p \left(C_{D_p} + C_{L_p}\tan\phi_{p_k\psi_{p_i}}^{V_t}\right)\Delta r_p, \quad k = 1, 2\ldots, 8 \\ M_{y_k} = \frac{1}{2m_n}\rho N\Omega_k^2 \sum_{i=1}^{m_n}\sum_{r_p=R_h}^{R} \frac{r_p^3\cos\psi_{p_i}}{\cos\phi_{p_k\psi_{p_i}}^{V_t}} c_p \left(C_{L_p} - C_{D_p}\tan\phi_{p_k\psi_{p_i}}^{V_t}\right)\Delta r_p, \quad k = 1, 2\ldots, 8 \end{cases} \tag{20}$$

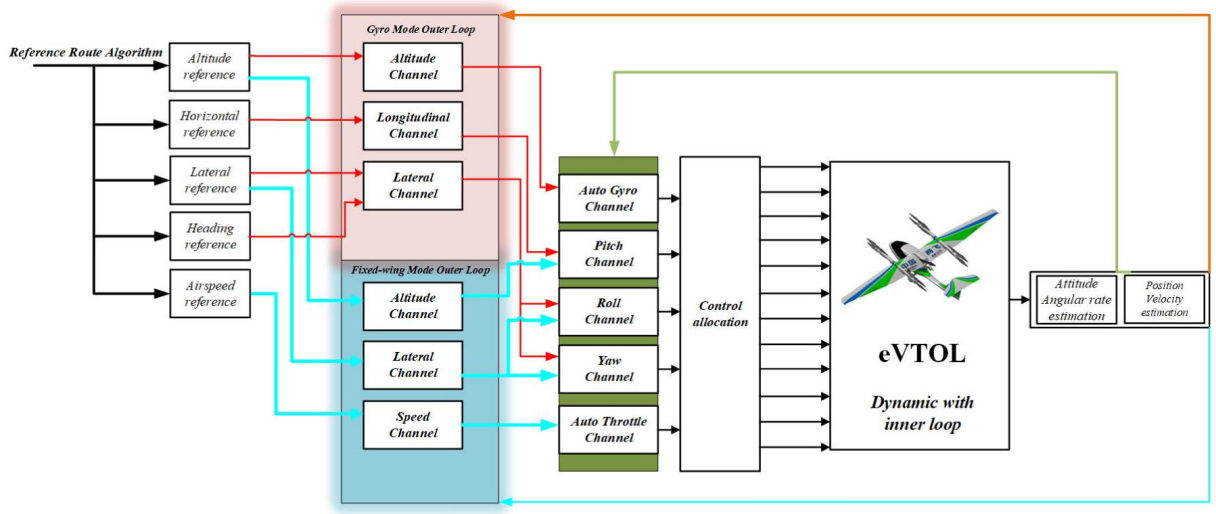

FIGURE 10. The complete control structure for ET120.

A. CONTROL LAW

The stabilization controller for the ET120 is composed of a three-axis roll, pitch, and yaw control stability augmentation system (CSAS). The CSAS generates virtual angular-rate acceleration control commands, and yielding moment instructions to the control allocator. The $\mathcal{L}_1$ adaptive controller has an edge over the PID controllers in the following aspects: 1) The performance of the PID controller relies strongly on the model precision; 2) The gain scheduling of the PID controller is complicated and an in-time adjustment is inaccessible during the flight, which may cause the vehicle out of control; 3) $\mathcal{L}_1$ adaptive controller is easy to achieve the level 1 flight quality even though the plant is not ascertained. So, a SISO $\mathcal{L}_1$ adaptive controller is designed for each of the three angular rate channels to compensate for unmatched uncertainties in the dynamics. For slow-loop design (e.g. pitch and roll angles), the NDI offers the tracking of the desired dynamics. By choosing the bandwidth of the $\mathcal{L}_1$ reference model (state predictor) at level 1 flying qualities according to military flight quality standards (e.g., MIL-STD-1797B), the desired closed-loop performance of the actual vehicle dynamics can be acquired. FIGURE 11 shows the complete control stability augmentation layer that uses NDI theory and $\mathcal{L}_1$ adaptive augmentation.

Owing to the similar control structures of the roll, pitch, and yaw channels, only the pitch channel is discussed here.

The pitch cascade channel decouples the angle and angular rate according to the principle of time-scale separation. The NDI approach is applied to the angle loop while $\mathcal{L}_1$ adaptive control is imposed on the angular rate. The $\mathcal{L}_1$ adaptive law can be divided into four parts: control plant, state predictor, adaptive law, and control law. To separate the control law from the adaptive law in the design phase, an improved approach, adding a low-pass filter to the control law, is involved in. In the next section, we describe the design of $\mathcal{L}_1$ adaptive law step by step [24]–[26].

1) DESIGN OF NDI CONTROLLER FOR PITCH LOOP

We first need to design the NDI controller for the pitch loop. The equation of pitch motion, Eq. (26), can be written as

$$\dot{\theta}(t) = f_1(\theta(t), t) + g_1(\theta(t), t)q(t) \tag{27}$$

where $f_1(\theta(t), t)$, $g_1(\theta(t), t)$ are affine functions with $f_1(\theta(t), t) = 0$ and $g_1(\theta(t), t) = 1$.

We define an error term $\Delta\theta(t) = \theta_c(t) - \theta(t)$, then the NDI controller is given as:

$$q_c(t) = g_1^{-1}(K_\theta \Delta\theta(t) - f_1(\theta(t), t)) \tag{28}$$

where the K_θ is the design gain of the pitch angle loop. In the following context, the definition of q_c and $q_c(t)$ is identical, so are the p_c (r_c) and $p_c(t)$ ($r_c(t)$).

2) DESIGN OF L1 ADAPTIVE CONTROLLER FOR PITCH RATE LOOP

a: CONTROL PLANT

According to small perturbation theory, the equation of pitch moment, Eq. (25), can be simplified to:

$$\dot{q}(t) = M_\alpha \alpha(t) + M_q q(t) + M_{\dot{q}_{uc}} \dot{q}_{uc}(t) \tag{29}$$

where $\dot{q}_{uc}(t)$ is the total virtual pitch angular acceleration, M_α and M_q are aerodynamic factors, and $M_{\dot{q}_{ac}}$ is the virtual control moment produced per unit of the virtual output signal $\dot{q}_{uc}(t)$. From Eq. (29), $\dot{q}_{uc}(t)$ can be expressed as:

$$\begin{aligned} \dot{q}_{uc}(t) &= \frac{1}{M_{\dot{q}_{uc}}}[\dot{q}_c(t) - M_\alpha \alpha(t) - M_q q(t)] \\ &= \dot{q}_{Tc}(t) + \dot{q}_{ac}(t) \end{aligned} \tag{30}$$

where $\dot{q}_{Tc}(t)$ and $\dot{q}_{ac}(t)$ are the pitch angular acceleration produced by aero-surfaces and hovering rotors, respectively. At low airspeed, the control moment contributions from hovering rotors are dominant while aero-surfaces are trivial. The hovering rotors deliver the desired pitch angular acceleration,

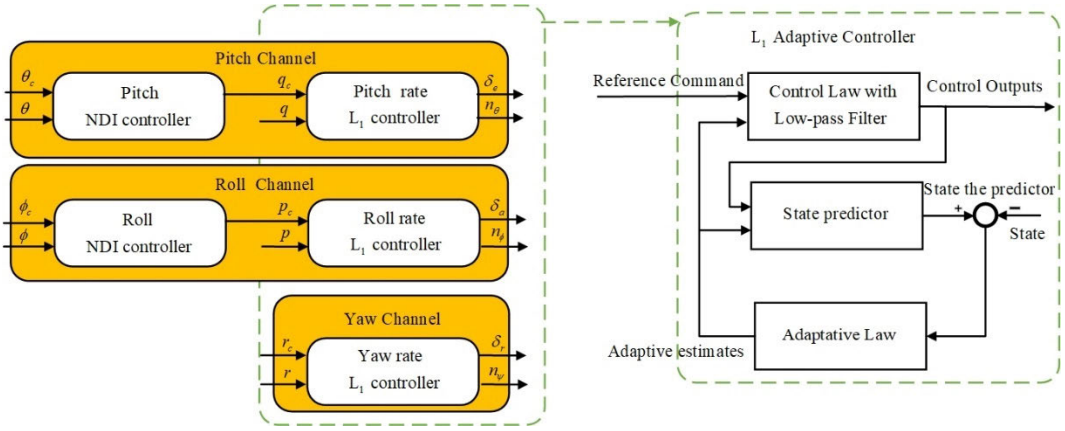

FIGURE 11. Flow chart of $\mathcal{L}_1$ adaptive controller, where q_c, p_c and r_c are the pitch, roll and yaw rate command, respectively, and θ_c and ϕ_c are the pitch and roll commands, respectively.

that is, $\dot{q}_{uc}(t) \triangleq \dot{q}_{Tc}(t)$, $\dot{q}_{ac}(t) \triangleq 0$. At high airspeed, the situation is reversed and the aero-surfaces undertake the required pitch angular acceleration, that is, $\dot{q}_{Tc}(t) \triangleq 0$, $\dot{q}_{uc}(t) \triangleq \dot{q}_{ac}(t)$. During transition flight, both the aero-surfaces and hovering rotors achieve the commanded pitch angular acceleration.

Considering the uncertainties of the pitch moment, Eq. (29) can be expressed as:

$$\dot{q}(t) = (M_\alpha + \hat{M}_\alpha)\alpha(t) + (M_q + \hat{M}_q)q(t) + (M_{\dot{q}_{uc}} + \hat{M}_{\dot{q}_{uc}})\dot{q}_{uc}(t) + \sigma_1 \quad (31)$$

We substitute Eq. (30) into Eq. (31) to get:

$$\dot{q}(t) = \hat{M}_\alpha\alpha(t) + \hat{M}_q q(t) + \frac{\hat{M}_{\dot{q}_{uc}}}{M_{\dot{q}_{uc}}}(\dot{q}_c(t) - M_\alpha\alpha(t) - M_q q(t)) + \dot{q}_c(t) + \sigma_1 \quad (32)$$

where $\hat{M}_\alpha$, $\hat{M}_q$ and $\hat{M}_{\dot{q}_{uc}}$ are uncertain aerodynamic factors and σ_1 is the disturbance factor. Then the first-order reference model is structured as:

$$\dot{q}(t) = -K_q q(t) + K_q q_c(t) \quad (33)$$

where K_q is the bandwidth of the pitch angular rate loop.

By combining Eq. (32) and Eq. (33), we can rewrite the control plant of the pitch channel as:

$$\begin{cases} \dot{q}(t) = -K_q q(t) + K_q \eta(t) \\ \eta(t) = \omega_q \dot{q}_c(t) + f_2(t, q(t)) \\ f_2(t, q(t)) = \theta_q(t)q(t) + \sigma_q(t) \end{cases} \quad (34)$$

where $\omega_q = 1 + \frac{\hat{M}_{\dot{q}_{uc}}}{M_{\dot{q}_{uc}}}$ is the virtual control factor, $\theta_q(t) = K_q - \frac{\hat{M}_{\dot{q}_{uc}}}{M_{\dot{q}_{uc}}}M_q$ is aerodynamic factors, and $\sigma_q(t) = -\frac{\hat{M}_{\dot{q}_{uc}}}{M_{\dot{q}_{uc}}}M_\alpha\alpha + \sigma_1$ is aerodynamic disturbance, $f_2\,(t, q\,(t))$ is affine function.

Assumption 4: The unknown constant ω_q is uniformly bounded, which confine in $[\omega_{ql}, \omega_{qu}]$, where ω_{ql} and ω_{qu} are the lower and upper bounds of ω_q.

In practical application, $[\omega_{ql}, \omega_{qu}]$ belongs to $[1/3, 3]$.

Assumption 5: $f_2(t, 0)$ in Eq. (34) is uniformly bounded, as $\|f_2(t, 0)\|_\infty \leq b$, with $b > 0$, where $\|\bullet\|_\infty$ is the ∞-norm.

Since that in practical application, angular rate is limited to a certain range, assumption 5 is easily satisfied.

Assumption 6: The partial derivative of f_2 is semi-globally uniformly bounded: For $\delta > 0$, there exist $d_{fq}(\delta) > 0$ and $d_{ft}(\delta) > 0$ independently of time to ensure that the partial derivative of $f_2(t, q(t))$ is piecewise continuous and bounded as:

$$\begin{cases} \left\| \dfrac{\partial f_2(t, q(t))}{\partial q} \right\|_\infty \leq d_{fq}(\delta), \\ \left\| \dfrac{\partial f_2(t, q(t))}{\partial t} \right\|_\infty \leq d_{ft}(\delta). \end{cases} \quad (35)$$

For the inner loop control system, the uncertainty possesses a certain magnitude and limit, so the assumptions 4-6 can be satisfied.

Lemma 1: For $\tau \geq 0$, if $\|q_\tau\|_{L_\infty} \leq \rho$ and $\|\dot{q}_\tau\|_{L_\infty} \leq d$, where ρ and d are positive constants, and $\theta_q(t)$ and $\sigma_q(t)$ are continuous [12]. In addition, their derivatives for $t \in [0, \tau]$ are

$$f(t, q(t)) = \theta_q(t)\,\|q_t\|_{L_\infty} + \sigma_q(t) \quad (36)$$

$$\left|\theta_q(t)\right| < d_{fq}(\rho), \left|\dot{\theta}_q(t)\right| \leq d_\theta \quad (37)$$

$$\left|\sigma_q(t)\right| < b, \left|\dot{\sigma}_q(t)\right| \leq d_\sigma \quad (38)$$

where d_θ and d_σ are calculable limits; $\|\bullet\|_{L_\infty}$ is the L_∞-norm.

The adaptive law controller is designed based on the above assumptions 4-6 and lemma 1. It includes state predictor, adaptive law, and control law.

b: STATE PREDICTOR

According to Eq. (34), the state predictor can be constructed as:

$$\begin{cases} \dot{\hat{q}}(t) = -K_q\hat{q}(t) + K_q\hat{\eta}(t) \\ \hat{\eta}(t) = \hat{\omega}_q(t)\dot{q}_c(t) + \hat{\theta}_q(t)q(t) + \hat{\sigma}_q(t) \\ \hat{y}(t) = \hat{q}(t) \end{cases} \quad (39)$$

where $\hat{\omega}_q(t)$ is the estimated uncertainty of the control factor, $\hat{\theta}_q(t)$ is the estimated uncertainty of the aerodynamic factor,

and $\hat{\sigma}_q(t)$ is the estimated uncertainty of aerodynamic disturbance.

c: ADAPTIVE LAW

The adaptive gains are governed by:

$$\begin{cases} \dot{\hat{\theta}}_q(t) = \Gamma K_{proj}(\hat{\theta}_q(t), -\tilde{q}(t)PK_q \|q(t)\|_\infty) \\ \dot{\hat{\sigma}}_q(t) = \Gamma K_{proj}(\hat{\sigma}_q(t), -\tilde{q}(t)PK_q) \\ \dot{\hat{\omega}}_q(t) = \Gamma K_{proj}(\hat{\omega}_q(t), -\tilde{q}(t)PK_q\dot{q}_c(t)) \end{cases} \tag{40}$$

where Γ is adaptive gain, $\tilde{q}(t) = \hat{q}(t) - q(t)$ is tracking error, P is the solution of the Lyapunov equation $-K_q^T P - PK_q = -Q$ and $Q > 0$. K_{proj} is the projection operator that can guarantee the boundedness of the adaptive parameters defined in Ref [27].

d: CONTROL LAW

The control law is generated as:

$$\begin{cases} \dot{q}_c = K_d D[K_g q(t) - \hat{\omega}_q(t)\dot{q}_c(t) - \hat{\theta}_q(t)q(t) - \hat{\sigma}_q(t)] \\ \dot{q}_{uc} = \dfrac{1}{M_{\dot{q}_{uc}}}[\dot{q}_c - M_\alpha \alpha(t) - M_q q(t)] \end{cases} \tag{41}$$

where K_g is adaptive feedback gain, D is a low-pass filter and K_d is the adaptive feed forward gain. The $\mathcal{L}_1$ adaptive control scheme is depicted in FIGURE 12. The design of control law should to be able to guarantee that the following transfer function is strictly regular:

$$C(s) = \omega_q K_d D(s)(I + \omega_q K_d D(s))^{-1} \tag{42}$$

Further $C(0) = I$, where I is the identity matrix.

The values of K_d and D also need to be set to ensure that for a given ρ_0, there exist $\rho_r > \rho_{in}$ to maintain the $\mathcal{L}_1$ norm condition:

$$\|G(s)\|_{L_1} < \frac{\rho_r - \left\|H(s)C(s)K_g\right\|_{L_1} \|q_c\|_{L_\infty} - \rho_{in}}{L_{\rho_r}\rho_r + b} \tag{43}$$

where $\|\bullet\|_{L_1}$ is the $\mathcal{L}_1$-norm, and

$$\begin{cases} \rho_{in} := \left\|s(sI + K_q)^{-1}\right\|_{L_1} \rho_0 \\ H(s) = (sI + K_q)^{-1}K_q \\ G(s) = H(s)[I - C(s)] \\ L_{\rho_r} = \dfrac{\rho_r + \bar{\gamma}_1}{\rho_r} d_{\mathrm{fq}}[\rho_r + \bar{\gamma}_1] \end{cases} \tag{44}$$

d_{fq} is defined in Eq. (35); $\bar{\gamma}_1$ is an arbitrary positive constant.

Once the $\mathcal{L}_1$-norm condition in Eq. (43) has been satisfied, the adaptive controller of the inner loop is constituted by Eqs. (39)-(41).

3) STABILITY ANALYSIS OF L1 ADAPTIVE CONTROLLER

The Lyapunov's second method is used to derive the stability of the adaptive controller, and involves constructing a Lyapunov function.

The actual plant and state predictor have been defined in Eqs. (34) and (39), respectively. Thus, the tracking error is constructed as:

$$\begin{cases} \tilde{q}(t) = \hat{q}(t) - q(t) \\ \dot{\tilde{q}}(t) = -K_q\tilde{q}(t) + K_q\tilde{\eta}(t) \end{cases} \tag{45}$$

where $\tilde{\eta}(t) = \hat{\eta}(t) - \eta(t)$. Then, following the Eq. (34), gives:

$$\begin{aligned} \tilde{\eta}(t) &= \hat{\eta}(t) - \eta(t) \\ &= \dot{q}_c(t)\tilde{\omega}_q(t) + q(t)\tilde{\theta}_q(t) + \tilde{\sigma}_q(t) \end{aligned} \tag{46}$$

with $\tilde{\omega}_q(t) = \hat{\omega}_q(t) - \omega_q(t)$, $\tilde{\theta}_q(t) = \hat{\theta}_q(t) - \theta_q(t)$ and $\tilde{\sigma}_q(t) = \hat{\sigma}_q(t) - \sigma_q(t)$. Substituting Eq. (46) into Eq. (45), yielding:

$$\dot{\tilde{q}}(t) = -K_q\tilde{q}(t) + K_q[\dot{q}_c(t)\tilde{\omega}_q(t) + q(t)\tilde{\theta}_q(t) + \tilde{\sigma}_q(t)] \tag{47}$$

The goal of adaptive laws is to drive the $\tilde{\omega}(t)$, $\tilde{\theta}(t)$ and $\tilde{\sigma}(t)$ tend to zero to achieve stable error dynamics $\dot{\tilde{q}}(t) = -K_q\tilde{q}(t)$.

Next, the candidate Lyapunov function is structured as:

$$V(\tilde{q}, \tilde{\omega}_q, \tilde{\theta}_q, \tilde{\sigma}_q) = \tilde{q}^T(t)P\tilde{q}(t) + \frac{1}{\Gamma}(\tilde{\omega}_q^2(t) + \tilde{\theta}_q^2(t) + \tilde{\sigma}_q^2(t)) \tag{48}$$

Taking the time derivative of Eq. (48) obtains:

$$\begin{aligned} \dot{V}(\tilde{q}, \tilde{\omega}_q, \tilde{\theta}_q, \tilde{\sigma}_q) = {} & \dot{\tilde{q}}^T(t)P\tilde{q}(t) + \tilde{q}^T(t)P\dot{\tilde{q}}(t) \\ & + \frac{2}{\Gamma}(\tilde{\omega}_q(t)\dot{\tilde{\omega}}_q(t) + \tilde{\theta}_q(t)\dot{\tilde{\theta}}_q(t) \\ & + \tilde{\sigma}_q(t)\dot{\tilde{\sigma}}_q(t)) \end{aligned} \tag{49}$$

We assume that the parameters ω_q, θ_q and σ_q vary so slowly that $\dot{\tilde{\omega}}_q \approx \dot{\hat{\omega}}_q$, $\dot{\tilde{\theta}}_q \approx \dot{\hat{\theta}}_q$, $\dot{\tilde{\sigma}}_q \approx \dot{\hat{\sigma}}_q$. Substituting Eq. (47) into Eq. (49), we get

$$\begin{aligned} &\dot{V}(\tilde{q}, \tilde{\omega}_q, \tilde{\theta}_q, \tilde{\sigma}_q) \\ &= \{-\tilde{q}^T(t)K_q^T + [\tilde{\omega}_q^T(t)\dot{q}_c^T(t) + \tilde{\theta}_q^T(t)q^T(t) + \tilde{\sigma}_q^T(t)]K_q^T\}P\tilde{q}(t) \\ &\quad + \tilde{q}^T(t)P\{-K_q\tilde{q}(t) + K_q[\dot{q}_c(t)\tilde{\omega}_q(t) + q(t)\tilde{\theta}_q(t) + \tilde{\sigma}_q(t)]\} \\ &\quad + \frac{2}{\Gamma}(\tilde{\omega}_q^T(t)\dot{\hat{\omega}}_q(t) + \tilde{\theta}_q^T(t)\dot{\hat{\theta}}_q(t) + \tilde{\sigma}_q^T(t)\dot{\hat{\sigma}}_q(t)) \end{aligned} \tag{50}$$

By using the projection-based adaptive laws in Eqs. (40) and (44) derives:

$$\begin{aligned} &\dot{V}(\tilde{q}, \tilde{\omega}_q, \tilde{\theta}_q, \tilde{\sigma}_q) \\ &= -\tilde{q}^T(t)Q\tilde{q}(t) \\ &\quad + 2\tilde{\omega}_q(t)(\tilde{q}^T(t)PK_q\dot{q}_c^T(t) + K_{proj}(\hat{\omega}_q(t), -\tilde{q}^T(t)PK_q\dot{q}_c(t))) \\ &\quad + 2\tilde{\theta}_q^T(t)(q(t)\tilde{q}^T(t)PK_q + K_{proj}(\hat{\theta}_q(t), -q(t) - \tilde{q}^T(t)PK_q)) \\ &\quad + 2\tilde{\sigma}_q^T(t)(\tilde{q}^T(t)PK_q + K_{proj}(\hat{\sigma}_q(t), -\tilde{q}^T(t)PK_q)) \\ &\quad - \frac{2}{\Gamma}(\tilde{\omega}_q^T(t)\dot{\omega}_q(t) + \tilde{\theta}_q^T(t)\dot{\theta}_q(t) + \tilde{\sigma}_q^T(t)\dot{\sigma}_q(t)) \end{aligned} \tag{51}$$

The projection operator in adaptive laws ensures that the adaptive parameters are limited to a known compact set Λ. The projection operator is given as $\dot{\theta}_q(t) = K_{proj}(\theta_q, \Gamma z)$, and the properties of the projection function guarantee that for any point $\theta_q(\tau_1) \in \Lambda$,where $\tau_1 \in [0, t)$ and z is a parameter. Then, we have:

$$(\theta_q - \theta_q(\tau_1))^T(\Gamma^{-1}K_{proj}(\theta_q, \Gamma z) - z) \leq 0 \tag{52}$$

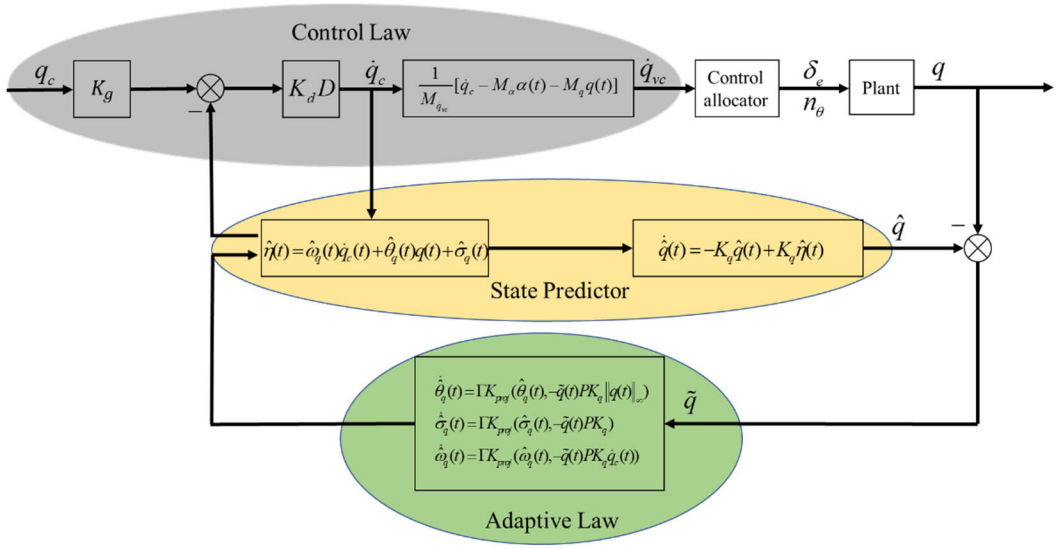

FIGURE 12. Block diagram of $\mathcal{L}_1$ adaptive controller.

According to the properties of projection functions, Eq. (51) can be simplified as:

$$\dot{V}(\tilde{q},\tilde{\omega}_q,\tilde{\theta}_q,\tilde{\sigma}_q) \leq -\tilde{q}^T(t)Q\tilde{q}(t)+\frac{2}{\Gamma}(\left|\tilde{\omega}_q^T(t)\dot{\omega}_q(t)+\tilde{\theta}_q^T(t)\dot{\theta}_q(t)+\tilde{\sigma}_q^T(t)\dot{\sigma}_q(t)\right|) \tag{53}$$

Since ω_q is a constant which yields $\dot{\omega}_q = 0$. Then, Eq. (53) can be expressed as:

$$\dot{V}(\tilde{q},\tilde{\omega}_q,\tilde{\theta}_q,\tilde{\sigma}_q) \leq -\tilde{q}^T(t)Q\tilde{q}(t) +\frac{2}{\Gamma}(\left|\tilde{\theta}_q^T(t)\dot{\theta}_q(t)+\tilde{\sigma}_q^T(t)\dot{\sigma}_q(t)\right|) \tag{54}$$

According to the bounds Eqs. (37)-(38) defined in Lemma 1, Eq.(54) is able to be simplified as:

$$\dot{V}(\tilde{q},\tilde{\omega}_q,\tilde{\theta}_q,\tilde{\sigma}_q) \leq -\tilde{q}^T(t)Q\tilde{q}(t)+\frac{4}{\Gamma}(d_{\mathrm{fq}}(\rho)d_\theta + bd_\sigma) \tag{55}$$

Using the properties of projection operator again, Eq. (48) is rewritten as:

$$\tilde{\omega}_q^2(t)+\tilde{\theta}_q^2(t)+\tilde{\sigma}_q^2(t)\leq(\omega_{qu}-\omega_{ql})^2+4d_{\mathrm{fq}}^2(\rho)+4b^2 \tag{56}$$

Considering that $\tilde{q}(0) = 0$ leads to

$$V(0) \leq \frac{1}{\Gamma}((\omega_{qu}-\omega_{ql})^2+4d_{\mathrm{fq}}(\rho)d_\theta+4bd_\sigma) \tag{57}$$

Assume that:

$$V(t) > \frac{\lambda_m(\rho_r)}{\Gamma} \tag{58}$$

where $\lambda_m(\rho_r) \triangleq (\omega_{qu}-\omega_{ql})^2+4d_{\mathrm{fq}}^2(\rho)+4b^2+4\frac{\lambda_{\max}(P)}{\lambda_{\min}(Q)}(d_{\mathrm{fq}}(\rho)d_\theta+bd_\sigma)$, $\lambda_{\max}(P)$ is the max eigenvalue of matrix P and $\lambda_{\min}(P)$ is the min eigenvalue of matrix Q.

Substitute Eq. (56) and Eq. (58) into Eq. (48):

$$\begin{aligned}\tilde{q}^T(t)Q\tilde{q}(t) &\geq \frac{\lambda_{\max}(Q)}{\lambda_{\min}(P)}\tilde{q}^T(t)P\tilde{q}(t)\\ &\geq \frac{4}{\Gamma}(d_{\mathrm{fq}}(\rho)d_\theta+bd_\sigma)\end{aligned} \tag{59}$$

Using Eqs. (59) and (55) yields $\dot{V}(\tilde{q},\tilde{\omega}_q,\tilde{\theta}_q,\tilde{\sigma}_q) < 0$ Therefore, we have:

$$\begin{aligned}V(t) &\leq V(0)\\ &\leq \frac{1}{\Gamma}((\omega_{qu}-\omega_{ql})^2+4d_{\mathrm{fq}}(\rho)d_\theta+4bd_\sigma)\\ &\leq \frac{\lambda_m(\rho_r)}{\Gamma}\end{aligned} \tag{60}$$

The result of Eq. (60) contradicts with the assumption of Eq. (52). The actual assumption of Eq. (58) should be rewritten as:

$$V(t) \leq \frac{\lambda_m(\rho_r)}{\Gamma} \tag{61}$$

It has been proven by Lyapunov's second method that the system tends to gradually stabilize. An the $\mathcal{L}_1$ adaptive control can ensure that the prediction error of the inner loop system is bounded. Meanwhile, by increasing Γ to reduce the prediction error but will reduce the robustness of the system, the choice of Γ should be a trade-off between performance and robustness.

The derived of the adaptive law by Lyapunov analysis leads to a bounded state error $\tilde{q} = \hat{q} - q$. However, it cannot prove the system absolute stability. For example, if both $\hat{q}$ and q diverge at the same rate, this results in a bounded state error $\tilde{q}$ but an unbounded state q. According to Ref. [14], [24], it is possible to illustrate that the reference system can be bounded if

$$\|H(s)[I-C(s)]\|_\infty < \frac{1}{\max_{\theta\in\Omega}\|\theta_q\|_{L_1}} \tag{62}$$

From the above analysis, it is clear that the prediction error of the inner loop can be guaranteed to be bounded by using the $\mathcal{L}_1$ adaptive controller.

4) PERFORMANCE BOUND ANALYSIS OF L1 ADAPTIVE CONTROLLER

Here, the performance bounds of the real plant relative to the reference system is discussed, which corresponds to the $\mathcal{L}_1$ adaptive controller defined in Eqs. (39)-(41):

$$\begin{cases} \dot{q}_{ref}(t) = -K_q q_{ref}(t) \\ \quad + K_q(\omega_q \dot{q}_{c_{ref}}(t) + \theta_q q_{ref}(t) + \sigma_q), \\ \dot{q}_{c_{ref}}(s) = \dfrac{C(s)}{\omega_q}(K_g q_c(s) - \eta_{ref}(s)), \\ y_{ref}(t) = q_{ref}(t). \end{cases} \tag{63}$$

where $\dot{q}_{c_{ref}}(s)$, $q_c(s)$ and $\eta_{ref}(s)$ are the Laplace transforms of $\dot{q}_{c_{ref}}(t)$, $q_c(t)$ and $\eta_{ref}(t)$, respectively.

We define $\bar{\rho}_r(\rho_r) = \rho_r + \bar{\gamma}_1$ where ρ_r and $\bar{\gamma}_1$ are given in Eq. (44); then, γ_1 is obtained as:

$$\gamma_1 = \frac{\|C(s)\|_{L_1}}{1 - \|G(s)\|_{L_1} L_{\rho_r}} \gamma_0 + \xi \tag{64}$$

where γ_0 and ξ are the arbitrarily small positive constants and $\gamma_1 \leq \bar{\gamma}_1$. Then, we have:

$$\rho_u = \rho_{ur} + \gamma_2 \tag{65}$$

ρ_{ur} and γ_2 in the formula are defined as:

$$\begin{aligned} \rho_{ur} &= \left\|\omega_q^{-1} C(s)\right\|_{L_1} (L_{\rho_r} \rho_r + b) \\ &\quad + \left\|\omega_q^{-1} C(s) K_g(s)\right\|_{L_1} \|q_c\|_{L_\infty} \end{aligned} \tag{66}$$

$$\begin{aligned} \gamma_2 &= \left\|\omega_q^{-1} C(s)\right\|_{L_1} L_{\rho_r} \gamma_1 \\ &\quad + \left\|\omega_q^{-1} C(s) H^{-1}(s)\right\|_{L_1} \gamma_0 \end{aligned} \tag{67}$$

For the closed-loop reference system we have:

$$\|q_0\|_{L_\infty} \leq \rho_0 \tag{68}$$

$$\left\|q_{ref\,\tau}\right\|_{L_\infty} \leq \rho_r \tag{69}$$

$$\left\|q_{c_{ref}\,\tau}\right\|_{L_\infty} \leq \rho_{ur} \tag{70}$$

Assumption 7: We consider the closed-loop system describes in Eq. (34), utilizing the $\mathcal{L}_1$ adaptive controller defined in Eqs. (39)-(41) and the $\mathcal{L}_1$-norm condition [25]. Then, the limits are acquired:

$$\|q\|_{L_\infty} \leq \bar{\rho}_r(\rho_r), \|\dot{q}_c\|_{L_\infty} \leq \rho_u, \|\tilde{q}\|_{L_\infty} \leq \gamma_0, \tag{71}$$

$$\left\|q_{ref} - q\right\|_{L_\infty} \leq \gamma_1, \left\|\dot{q}_{c_{ref}} - \dot{q}_c\right\|_{L_\infty} \leq \gamma_2, \tag{72}$$

$$\left\|y_{ref} - y\right\|_{L_\infty} \leq \gamma_1 \tag{73}$$

where $\bar{\rho}_r(\rho_r)$, ρ_u, γ_1 and γ_2 are defined in Eqs. (38) and (64), respectively.

If the assumption defined in Eq. (63), for continuous $q(t)$, $q_{ref}(t)$, $\dot{q}_c(t)$ and $\dot{q}_{c_{ref}}(t)$ and $\left\|q_{ref}(0) - q(0)\right\|_\infty = 0 < \gamma_1$, $\left\|\dot{q}_{c_{ref}}(0) - \dot{q}_c(0)\right\|_\infty = 0 < \gamma_2$ holds, there must be an instant τ such that $\left\|q_{ref}(\tau) - q(\tau)\right\|_\infty = \gamma_1$ and $\left\|\dot{q}_{c_{ref}}(\tau) - \dot{q}_c(\tau)\right\|_\infty = \gamma_2$, where for $t \in [0, \tau)$, $\left\|q_{ref}(\tau) - q(\tau)\right\|_\infty < \gamma_1$, $\left\|\dot{q}_{c_{ref}}(\tau) - \dot{q}_c(\tau)\right\|_\infty < \gamma_2$ and $\|q_\tau\|_{L_\infty} < \bar{\rho}_r(\rho_r)$ and $\|\dot{q}_{c\tau}\|_{L_\infty} < \gamma_1$. Therefore, we have:

$$\left\|(q_{ref} - q)_\tau\right\|_{L_\infty} = \gamma_1, \left\|(\dot{q}_{c_{ref}} - \dot{q}_c)_\tau\right\|_{L_\infty} = \gamma_2 \tag{74}$$

It also needs to be satisfied as:

$$\|\tilde{q}_\tau\|_{L_\infty} < \gamma_0 \tag{75}$$

Hence, the system described in Eq. (34) can be expressed in complex field.

$$q(s) = G(s)\eta(s) - H(s)C(s)\tilde{\eta}(s) + H(s)C(s)K_g q_c(s) \tag{76}$$

By combining the Eqs. (63) and (76), we get:

$$q_{ref}(s) - q(s) = G(s)[\eta_{ref}(s) - \eta(s)] + H(s)C(s)\tilde{\eta}(s) \tag{77}$$

Then,

$$\begin{aligned} \left\|(q_{ref} - q)_\tau\right\|_{L_\infty} &\leq \|G(s)\|_{L_1} \left\|[\eta_{ref}(s) - \eta(s)]_\tau\right\|_{L_\infty} \\ &\quad + \|C(s)\|_{L_1} \|\tilde{q}(s)\|_\infty \end{aligned} \tag{78}$$

For $t \in [0, \tau]$, by using Eq. (78) yields:

$$\eta_{ref}(t) - \eta(t) = f_2(t, q_{ref}(t)) - f_2(t, q(t)) \tag{79}$$

Subtracting Eq. (78) from Eq. (79) results in:

$$\begin{aligned} \left\|(q_{ref} - q)_\tau\right\|_{L_\infty} &< \|G(s)\|_{L_1} L_{\rho_r} \left\|(q_{ref} - q)_\tau\right\|_{L_\infty} \\ &\quad + \|C(s)\|_{L_1} \|\tilde{q}_\tau\|_{L_\infty} \end{aligned} \tag{80}$$

Considering the $\mathcal{L}_1$-norm condition in Eq. (43) and the limit in Eqs. (75) and (80):

$$\left\|(q_{ref} - q)_\tau\right\|_{L_\infty} \leq \frac{\|C(s)\|_{L_1}}{1 - \|G(s)\|_{L_1} L_{1\rho_r}} \gamma_0 \tag{81}$$

Using γ_1 in Eq. (64), gives:

$$\left\|(q_{ref} - q)_\tau\right\|_{L_\infty} < \gamma_1 - \xi < \gamma_1 \tag{82}$$

Further, we have:

$$\dot{q}_{c_{ref}}(s) - \dot{q}_c(s) = -C(s)[\eta_{ref}(s) - \eta(s)] + C(s)\tilde{\eta}(s) \tag{83}$$

Respecting the limits in Eq. (82) and (83), yields:

$$\begin{aligned} \left\|(\dot{q}_{c_{ref}} - \dot{q}_c)_\tau\right\|_{L_\infty} &< \|C(s)\|_{L_1} L_{\rho_r}(\gamma_1 - \xi) + \|H(s)\|_{L_1} \gamma_0 \\ &< \gamma_2 \end{aligned} \tag{84}$$

where γ_2 is defined in Eq. (67).

The conclusions obtained in Eqs. (82) and (84) are contradictory to Eqs. (71) and (72). We prove the limits by the reduction and absurdum in Eq. (82) and prove the conclusion in Eq. (72) [16]. Given the equation $y_{ref}(t) - y(t) = [q_{ref}(t) - q(t)]$, the limits in Eq. (73) are also correct, which proves the assumption 7.

B. CONTROL ALLOCATION

The control allocator uses the desired angular acceleration and an estimate of the nominal control efficiency to determine the actuator's commands. Practical control allocation criteria can be acquired from Refs. [28], [29]. For the configuration of ET120, the number of virtual control inputs is smaller than the number of actual actuators. Usually, the pseudoinverse [28] methods can be applied to acquire the minimum deviation between the attained and the desired angular accelerations; However, it is unable to adapt directly to the ET120 for the inconsistent dynamic response of actuators (multi-rotors and aero-surfaces). Thus we designed a practical parallel control allocation criterion whose main principle is to assign the desired angular acceleration based on the capabilities of the aero-actuators and multi-rotors. The motion-related features of ET120 are almost symmetrical in its body axes, for that its inertia products can be ignored. Then, as shown in FIGURE 10, the virtual commands of the pitch, roll and yaw channels, $\dot{q}_{uc}$, $\dot{p}_{uc}$ and $\dot{r}_{uc}$, respectively, to the aero-actuators and multi-rotors are given as:

$$\begin{cases} \delta_e = \dfrac{\dot{q}_{uc}}{M_{\max}} \delta_e^{\min} \\ n_\theta = \dfrac{q_{uc}}{M_{\max}} n_\theta^{\max}, \end{cases} \begin{cases} \delta_a = \dfrac{\dot{p}_{uc}}{L_{\max}} \delta_a^{\min} \\ n_\phi = \dfrac{p_{uc}}{L_{\max}} n_\phi^{\max}, \end{cases} \begin{cases} \delta_r = \dfrac{\dot{r}_{uc}}{N_{\max}} \delta_r^{\max} \\ n_\varphi = \dfrac{\dot{r}_{uc}}{N_{\max}} n_\phi^{\max} \end{cases} \tag{85}$$

where $M_{\max}$, $L_{\max}$ and $N_{\max}$ are the maximum control efficiencies in the pitch, roll, and yaw channels, with

$$\begin{cases} M_{\max} = \eta_{\delta_e} \bar{M}_{\delta_e} \delta_e^{\min} + \bar{M}_{n_\theta} n_\theta^{\max} \\ L_{\max} = \eta_{\delta_a} \bar{L}_{\delta_a} \delta_a^{\min} + \bar{L}_{n_\phi} n_\phi^{\max} \\ N_{\max} = \eta_{\delta_r} \bar{N}_{\delta_r} \delta_r^{\max} + \bar{N}_{n_\varphi} n_\varphi^{\max} \end{cases} \tag{86}$$

where $\bar{M}_{n_\theta}$, $\bar{L}_{n_\phi}$, and $\bar{N}_{n_\varphi}$ are the pitch-, roll-, and yaw-related control efficiencies of the multi-rotors; $\bar{M}_{\delta_e}$, $\bar{L}_{\delta_a}$, and $\bar{N}_{\delta_r}$ are the pitch, roll, and yaw angular acceleration produced per unit of the aero-surfaces, and η_{δ_e}, η_{δ_a}, and η_{δ_r} are the gain-scheduling factors that vary with dynamic pressure, given as:

$$\eta_{\delta_e,\delta_a,\delta_r} = \begin{cases} 0 & 0 \le V_t \le V_1 \\ \left(\dfrac{V_t - V_1}{V_2 - V_1} \right)^2 & V_1 \le V_t \le V_2 \\ 1 & V_2 \le V_t \end{cases} \tag{87}$$

where V_1 and V_2 are the relative airspeeds of η_{δ_e}, η_{δ_a} and η_{δ_r} for gain-scheduling.

Moreover, in the transition flight process, the elevator should be prioritized over the multi-rotors to trim flight. This trim moment is a low-frequency signal due to the aerodynamics that can be extracted from the frequency domain. Therefore, a trim filter, also called the low-pass filter, is introduced to prioritize the elevator. By designing the closed short-period dynamics of ET120 at level 1 flying qualities, the low-frequency (trimming) pitch rate acceleration is first utilized by the elevator through the trim filter, while the high-frequency pitch rate acceleration naturally leaks into the rotors. Thus, the desired low-frequency pitch angular acceleration designates elevator as primary effector and treats hovering rotors as auxiliary effector which is used only when the elevator primaries saturate while the desired high-frequency pitch angular acceleration is allocated to the remaining elevator and hovering rotors in parallel according to Eq. (85). The flowchart of the control allocator of pitch channel is illustrated in FIGURE 13.

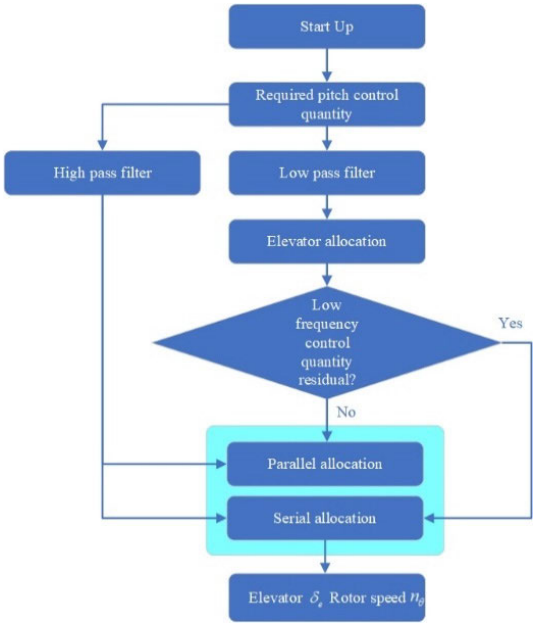

FIGURE 13. Flowchart of control allocator for pitch channel.

C. FLIGHT MANAGEMENT STRUCTURE

The flight management structure (FMS) provides the functions of navigation management, waypoint management, and multiple flight mode management. To satisfy the requirements of various flight modules and tests in various stages of development, a layered design of the architecture for flight management is created. The FMS for the ET120 platform is divided into four management levels, as shown in FIGURE 14. Each level is designed to make sure that the previous level supports it to mitigate risk.

The content of the levels of main FMS is as follows:

Level 1

Level 1 is composed of the standby mode, xbit mode, and operator mode, all of which are operated on the ground. The xbit mode is designed to test the mechanical and electronical systems of the ET120, including the aero-surfaces, rotors, and

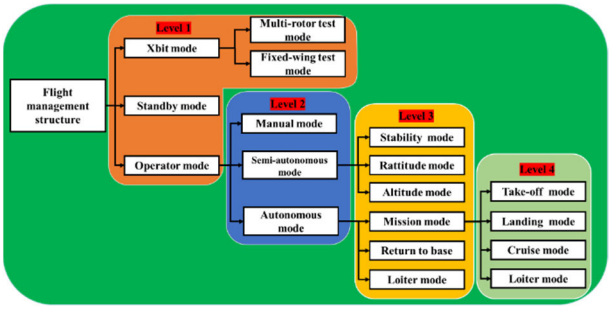

FIGURE 14. Flowchart of flight management structure.

the state of the sensors. The standby mode sets the status of the ET120 armed, restrains the aero-surfaces in the trim state and refuses remote operations. The operator mode sets the ET120 disarmed, and allows the autopilot to enter Level 2.

Level 2

Level 2 is based on the operator mode. In this layer, the control form, including the manual mode, the semi-autonomous mode and the autonomous modes, is determined. In the manual mode, absolute control authority is given to the receiver and the ground control station (GCS), where the ground operator can drive the aero-surfaces and rotors directly through operation instructions. The semi-autonomous mode sets the ET120 in the stability, r-attitude, or altitude mode. The ground operator provides the attitude, velocity, or altitude instructions directly to verify the control performance of the inner loop. The autonomous mode gives absolute control authority to the autopilot, which executes the control logic according to the internal program instructions in Level 3 and Level 4 to control the ET120 to autonomously complete the entire fight mission.

Level 3 and level 4

Level 3 supplies the specific operator mode according to the choice of semi-autonomous and autonomous modes in the layer. The stability mode, r-attitude mode, and altitude mode are based on the semi-autonomous mode. In the stability mode, the control instructions in the roll, pitch, and yaw channels represent the real attitude while the throttle channel directly controls rotor speed. The r-attitude mode is almost identical to the stability mode, except in terms of the throttle channel, where the r-attitude mode controls the rate of climb of ET120. In altitude mode, ET120 is controlled in the hovering state. The mission mode, return-to-base mode, and loiter mode are based on the autonomous mode. In the mission mode, the autopilot guides the ET120 to follow a mission route composed of waypoints. The type of waypoints is identified as the flight mode in Level 4, and is divided into the take-off mode, landing mode, cruise mode, and loiter mode. The return-to-base mode is designed to abort the mission and force the ET120 to return to the home position. The loiter mode enables the ET120 to infinitely loiter. The major functions provided by the mission mode of the FMS include navigation management, execution of

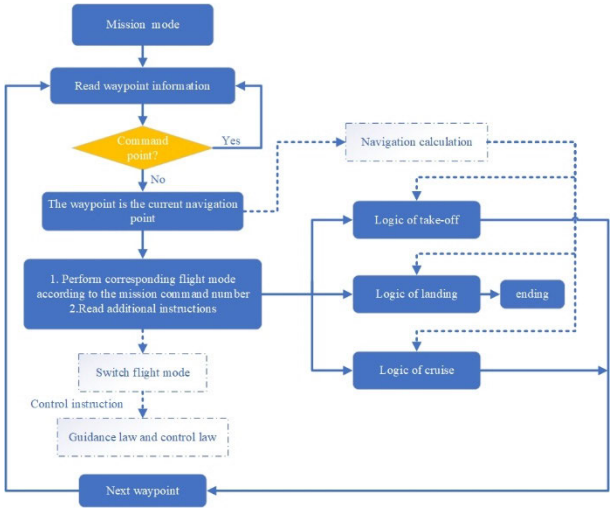

FIGURE 15. Flowchart of execution logic of mission mode.

additional waypoint commands, switching of waypoints, and control logics. The flowchart of the mission mode of the FMS is shown in FIGURE 15. In this mode, the waypoints can be divided into navigation and instruction points. The flight mode (e.g., the take-off, landing, and cruise modes) is tied to the navigation point. If the given waypoint is used for navigation, the internal control logic and corresponding flight mode are directly activated and executed according to the type of navigation point. The navigation management unit calculates the positional error between the ET120 and the flight route for the logical judgement and guidance loop. The activated flight mode advances to the next waypoint once it has completed the control logic, except for the landing mode. If the given waypoint is an additional instruction, the FMS passes them to the flight modes through the message mechanism of SIMULINK/Stateflow.

1) LOGIC OF TAKE-OFF

The strategy for fast accelerate transition maneuver design is based on the hybrid configuration of ET120. The available strategies include the following:

1. Only the propulsion rotor is used to provide forward acceleration, while the hovering rotors are used to maintain the pitch angle at zero as well as the flight altitude.
2. The hovering rotors maintain a fixed negative pitch angle to product the pitch-down motion, while the propulsion rotor is set to the maximum throttle.
3. The hovering rotors are used to control forward flight speed by adjusting the pitch angle, while the propulsion rotor is set to the maximum throttle.

The advantage of strategy 1 is that as the forward speed of the vehicle increases, the wing can provide all the aero-lift while the speed of the hovering rotors eventually drops to zero, which makes it possible to switch from the transition phase to level-flight without a significant drop in height.

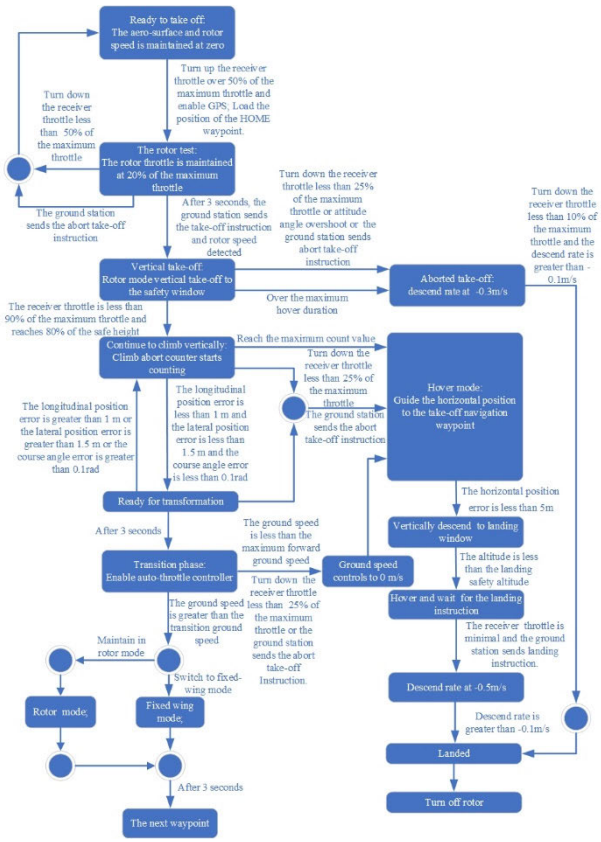

FIGURE 16. Flowchart of take-off logic.

However, a shortcoming of strategy 1 is that, the forward acceleration is limited owing to the limited power of the propulsion rotor and increase in the induced drag. Strategy 2 maximizes the release of the capability for forward acceleration. Its advantage is that both the propulsion rotor and the hovering rotors are used to provide forward acceleration, but a disadvantage is that the choice of negative pitch angle (zero-lift angle of attack) prevents the wing body from providing most of the lift, which increases the load and power consumption of the hovering rotors. This also leads to a severe drop in height owing to the larger pitch-down motion when switching to fixed-wing flight. Strategy 3 combines the advantages of strategies 1 and 2 and is used here. The propulsion rotor and hovering rotors together provide the forward acceleration, and the closed-loop control of the forward speed weakens the pitch-down trend with increasing forward speed. This in turn diminishes the altitude drop caused by module transition.

A flowchart of the take-off logic is shown in FIGURE 16. Before the ET120 is ready to take-off, it sets the aero-surfaces and rotor speed to zero. When the receiver throttle is turned up to over 50% of the maximum throttle, the rotor is turned on and its throttle is set to 20%. If the receiver throttle is turned down to less than 50% or the ground station sends the instruction to abort take-off, it returns to the ''ready take-off'' status. If the receiver throttle is kept above 50% for 3 s and the take-off instruction sent by the ground station is received, it begins vertical take-off. When it approaches 80% safety altitude, it hovers in the safety window to detect the throttle states of the receiver. If they are above 25% and less than 90% of the maximum throttle, it continues to climb vertically. The ''climb abort counter'' starts counting. When it approaches cruise altitude, it hovers and gets ready for transformation. The error in the longitudinal position less than 1 m, that in the lateral position error less than 1.5 m, and the course angle error is less than 0.1 rad, having been maintained for 3 s; it then switches to acceleration transition mode. During vertical climbing or conversion, the flight mode is converted into fixed-wing cruise mode when the ground speed approaches the transition speed. With regard to the various risks in the take-off phase, the protection logic aborts the ET120's nominal take-off logic and forces it into abort-take-off logic by turning down the receiver throttle to less than 25% or the ground station sends an abort-take-off instruction. The ET120 vertically lands at the take-off point at a rate of -0.5 m/s.

2) LOGIC OF LANDING

From the perspective of energy dissipation, the deceleration transition phase can be regarded as reducing the ET120's kinetic energy to zero. The idea is to transform the kinetic energy to potential energy by increasing the altitude. The corresponding maneuver design involves maintaining a constant pitch-up motion. The altitude then increases with decreasing airspeed. When the airspeed is low enough, the ET120 returns to stationary hovering.

A flowchart of the landing logic is shown in FIGURE 17. If the ET120 approaches the landing point in fixed-wing mode, the rotor is turned on, its throttle is set to 20% of the maximum throttle, and the auto-throttle controller is turned off. After holding this state for 3 s at an airspeed lower than the minimum safety airspeed, the ET120 switches to multi-rotor gyro mode. The protection logic forces the ET120 to go around in fixed-wing cruise mode by turning on the throttle to over 90% of the maximum throttle.

The deceleration transition phase is complete when the ground speed is less than the maximum forward ground speed; then, the hover mode is engaged to guide the horizontal position to the landing waypoint. When the horizontal position of the ET120 with respect to the landing waypoint is less than three meters, it begins to vertically descend to the landing window. If its horizontal distance from the landing waypoint is more than three meters, it stops descending for horizontal positional correction. After 3 s of maintaining an altitude lower than the safety landing altitude, it hovers in the landing window and waits for the landing instructions. Once the receiver throttle has been turned down to less than 10% of the maximum throttle and the ground station sends landing instructions, the ET120 lands automatically on the landing waypoint.

3) LOGIC OF CRUISE

A flowchart of the cruise logic is shown in FIGURE 18. The autopilot guides the ET120 to the next waypoint when its

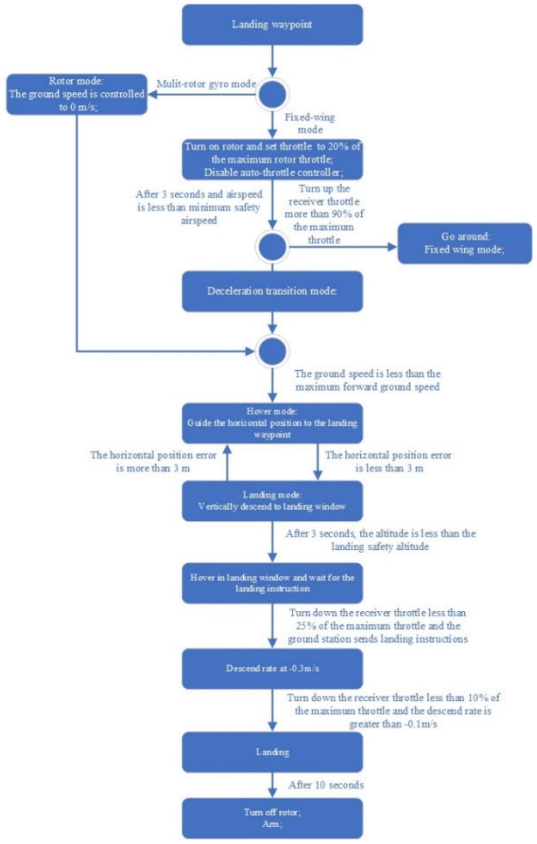

FIGURE 17. Flowchart of landing logic.

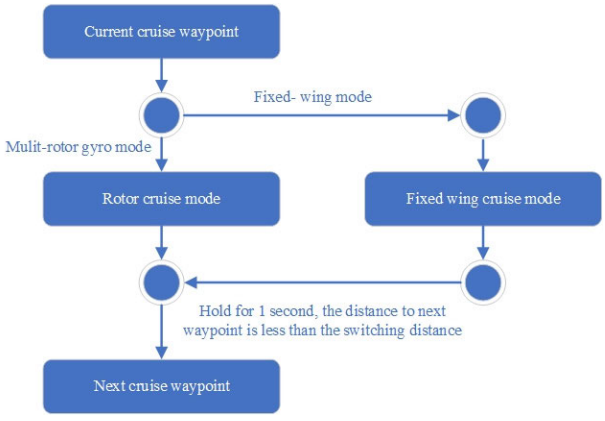

FIGURE 18. Flow chart of cruise logic.

distance to the waypoint is less than the switching distance, and maintains this state for 1 s. In addition, the cruise logic supports both rotor and fixed-wing cruise modes.

IV. EXPERIMENTAL RESULTS

A. VERIFICATION OF BEMT

As the calculations for the upper and lower rotors are roughly the same, only those for the upper rotor are provided in this section. First, a total of 12 blade elements were intercepted from 5% to 95% of the half-length of the rotor through

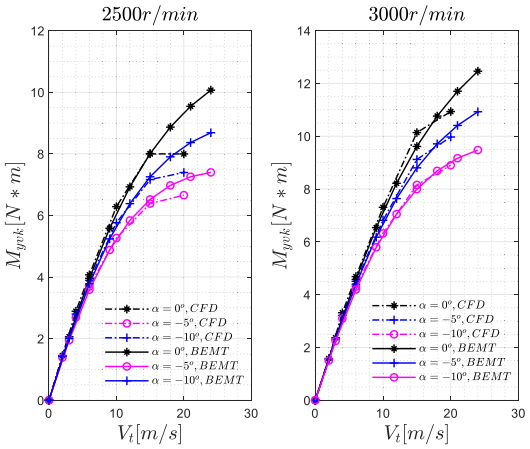

FIGURE 19. Comparison of overturning moments between CFD and the BEMT at different rotor speeds.

CATIA software. Second, XFOIL software was used to calculate the lift–drag characteristics of each element under a Reynolds number of 11,0000. Third, Eq. (20) was used to calculate the thrust, torque, and overturning moment at ranges of $-10°$ $\sim 10°$ of the angle of attack, 0$\sim$25 m/s of inflow speed, and 2500$\sim$3000 r/min of rotor speed. We used computational fluid dynamics (CFD) technology to calculate the thrust and overturning moment under the same forward ratio and inflow angle. The commercial CFD solver FLUENT was used for the numerical simulation, employing RANS with the SST $k-\omega$ turbulence model for closure. The additional overturning moment was more prominent when using BEMT theory, and significantly affects the characteristics of longitudinal trim. The results of the overturning moment in CFD and the BEMT method at rotor speeds of 2500 and 3000 r/min are shown in FIGURE 19. The following conclusion was obtained: First, the results of calculation of the BEMT method were similar to those of CFD, which verified the correctness of the BEMT method. Second, the overturning moment was positively related to the inflow speed, rotor speed, and inflow angle. Third, at a high inflow speed, the incremental overturning moment slowed down and stabilized. The rotor model based on the BEMT was thus suitable for the dynamic modeling of ET120.

B. MONTE CARLO SIMULATIONS

The tracking performance and the robustness of the designed $\mathcal{L}_1$ controller are verified by Monte Carlo simulations in the MATLAB/SIMULINK simulation environment. We design the $\mathcal{L}_1$ FCS abiding by the following control specifications both in hovering and forward-flight:

1. Level 1 flying qualities;
2. Time-delay margin greater than 100ms;
3. Gain margin greater than 6dB;
4. The static error of the step response in within 5%.

Table 1 lists the control parameters chosen for the desired closed-loop dynamics. These parameters for control

TABLE 1. Design dynamics for L1 FCS both in hovering and forward flight.

Design Parameters	Value
The desired pitch loop dynamics(s)	1
The desired roll loop dynamics(s)	0.5
Time constant for pitch rate loop(s)	1/6
Time constant for roll rate loop(s)	1/8
Time constant for yaw rate loop(s)	1/3

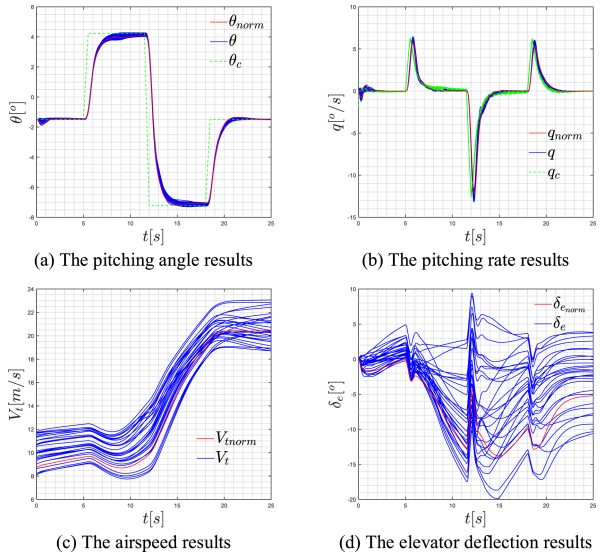

(a) The pitching angle results (b) The pitching rate results

(c) The airspeed results (d) The elevator deflection results

FIGURE 20. The longitudinal Monte Carlo simulation results in hovering mode.

specification, which satisfy the criterion held up by the forward flight and hovering flying quality, are determined for the best robustness and rapidity. Although there is a deviation in the short-period, roll, and Dutch roll modes between hovering and forward flight, the $\mathcal{L}_1$ controller can provide consistent closed-loop dynamics across the entire flight envelope with no scheduling by choosing the fixed time constant for the inner-loop state predictors. We choose the $\mathcal{L}_1$ controller adaptive gain as$\Gamma = 2500$ and the low-pass filter as $D = 1/s$. The bandwidth of inner loop controller is followed as Table 1.

FIGURE 20 and FIGURE 21 shows the simulation results in longitudinal channel. From FIGURE 20(a) and FIGURE 21(a), we have found that the tracking performance of the pitching angle is outstanding and that both in forward flight mode and hovering mode the response of pitching angle shows consistency. That means the $\mathcal{L}_1$ controller guarantees a stable and predictable dynamic characteristic in longitudinal channel no matter what control methods are chosen (see FIGURE 20(d) and FIGURE 21(d), the control methods are different). In forward flight mode the pitching angle is instinctively coupled with the climb rate, but in hovering mode, the climb rate is independently controlled by the total rotor speed of the hovering rotors, and the pitching angle is controlled by the rotor speed discrepancy of the front rotor and back rotor.

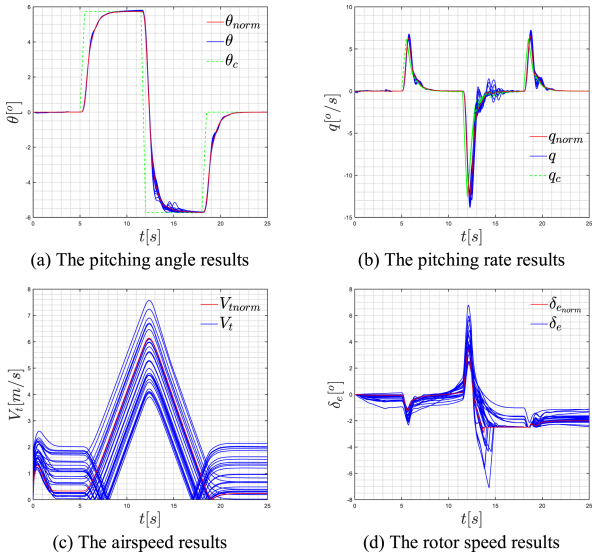

(a) The pitching angle results (b) The pitching rate results

(c) The airspeed results (d) The rotor speed results

FIGURE 21. The lateral Monte Carlo simulation results in forward-acceleration mode.

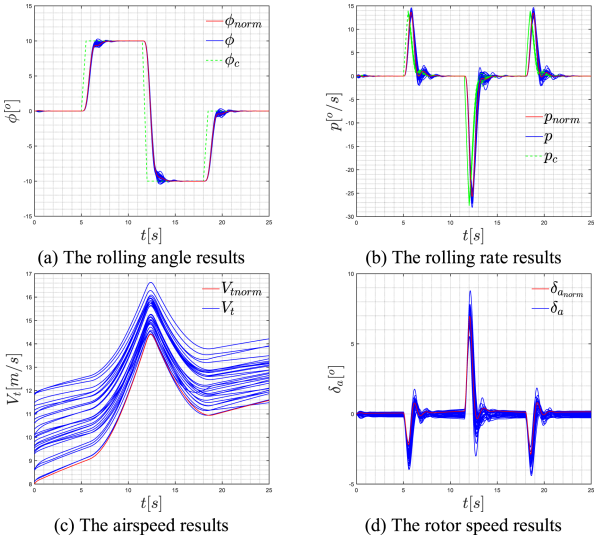

(a) The rolling angle results (b) The rolling rate results

(c) The airspeed results (d) The rotor speed results

FIGURE 22. The lateral Monte Carlo simulation results in forward-acceleration mode.

In the lateral channel, FIGURE 22 shows the forward acceleration mode results. In this mode both the aerodynamic surfaces and the rotor speed are involved in the lateral control strategy. FIGURE 22(a) (b)shows that in transitional mode the $\mathcal{L}_1$ controller still provides an excellent tracking performance. We have found that the control inputs vary simultaneously, the different amplitude direction is caused by the control input definition, which makes no difference in actual control inputs. See FIGURE 22(d), you can find that the left and right rotor speed vary oppositely with the control inputs, and the rolling control inputs agrees with the left rotor. This is physically reasonable, for that the left rotor speedup and right rotor speed down makes the fight bank to the right side, which induced a positive bank angle.

TABLE 2. Geometric parameters of the model of the virtual flight test.

Geometric parameters	Value
Reference area (m^2)	0.12
Wing span (m)	0.12
Mean aerodynamic chord (m)	1.2
Mass (k_g)	4.92
Rotational inertia of the x_b -axis($k_g \cdot m^2$)	0.28

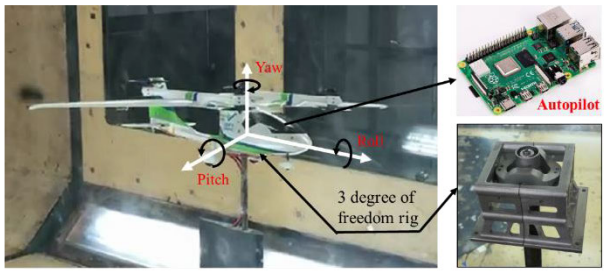

FIGURE 23. A 16.67%-scale model of the virtual flight test of ET120 in the NH-2 low-speed wind tunnel.

To conclude, either in longitudinal channel or in lateral channel, the results demonstrate that the designed $\mathcal{L}_1$ controller performs well when the plant is exposed to an empirical perturbation and that either in fixed-wing mode or multi-rotors mode or the transition mode the controlled plant displays a consistent tracking performance. The actuators are also controlled inside their saturation envelope, which means that the designed controller is highly efficient.

C. VIRTUAL FLIGHT TEST

The tracking performance of the $\mathcal{L}_1$ adaptive controller and the characteristics of flight trim have been verified by the Monte Carlo simulations above. However, a discrepancy between the simulation and the empirical model is generally obtained, which arises from the complex aerodynamic forces introduced by the rotor system modeling. Before prototyping the model into production and testing the algorithms in real flight, a virtual flight test was implemented to evaluate the tracking performance of the algorithms as well as the flight characteristics. A virtual flight-testing model was built to simulate the process of the transition phase. The test was carried out in the NH-2 low-speed wind tunnel at Nanjing University of Aeronautics and Astronautics (NUAA). The dimensions of the test section were 3 m $\times$ 2.5 m, and the maximum steady incoming flow was maintained at 90 m /s. 3D printing technology was used to manufacture the test model. A micro-motor power system was installed for gyro mode control and a micro-servo mechanism was installed for fixed-wing mode control. A magnetic encoder system was mounted on the axis of rotation of the aero-surface to measure the angle of the rudder through an analog-to-digital converter (ADC). An autopilot based on Raspberry Pi was embedded into the test model; it integrates the functions of signal acquisition, attitude estimation, control stability augmentation, and data logging. The angular rate was measured by a high-precision inertial sensor embedded in the autopilot, and the attitude angles (roll, pitch, and yaw) were estimated by an extended Kalman filter (EKF). The model of the virtual flight test and its installation are shown in FIGURE 23. A multi-bearing three-DOF support mechanism was manufactured in the test model to realize the rotation of the roll and pitch axes by $\pm 60°$, and that of the yaw axis at any angle. The size ratio of the test model to the flight model was 6:1, and the corresponding geometric parameters are shown in Table 2.

The tests examined the characteristics of flight trim, hovering anti-crosswind rejection capability, and the tracking performance the acceleration and deceleration transition modes. An experimental examination of the attitude response at various incoming flows validated the overall flight tasks. A pre-defined set of set-point commands was sent to the autopilot through the GCS to enable the test model to execute the corresponding attitude-related action. A video showing the tracking performance is available at (https://www.youtube.com/watch?v=XCRWvHmeiak), and the main flight tasks were as follows:

TEST 1–**Hovering tracking performance test**: A set of pre-defined commands were used to verify the tracking performance of the pitch, roll, and yaw controllers in a state of windless hovering. In this process, the support mechanism allowed for one-DOF to be released while the others were locked for the single-axis set-point test before three-DOF were controlled. During the test, the throttle of the rotor was set at 100% hovering speed and the incoming flow speed was $0m/s$.

Firstly, the tracking performance of the $\mathcal{L}_1$ controller is verified by a comparison experiment with an NDI controller. This experiment targets at the robustness performance verification. The robustness performance is reflected by the tracking performance of the controller when the plant is exposed to an external disturbance or the uncertain error between the actual model and the virtual plant. It is known that an NDI controller can ensure an excellent tracking performance in the nominal state, so to make a fair comparison, the NDI controller is tuned to have a same time domain tracking performance as the $\mathcal{L}_1$ controller, and then they are applied to the same protype vehicle, respectively. Then a same disturbance is imposed on the plant, which is ensured by fixing a cola bottle to the nose of the protype gently when the attitude of the protype is stable. The results of the experiment is shown in FIGURE 24, when time is over 18s the perturbance is activated, and an explicit discrepancy between the tracking performance of the two controllers are observed. The results verify that the $\mathcal{L}_1$controller has a superior tracking performance than that of the NDI controller.

TEST2–**Hovering anti-crosswind tracking performance test:** The model was initially in hovering mode, with the azimuth angle along the direction of the incoming

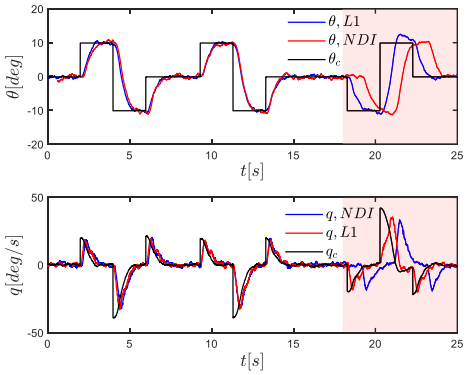

FIGURE 24. The pitch angle tracking performance of the $\mathcal{L}_1$ controller and NDI controller.

flow. The maximum anti-crosswind capability could be observed when wind tunnel was operating. In this process, the support mechanism allowed for three-DOF to be released, the throttle of the rotor was set to 100% hovering speed, and the incoming flow speed was increased from 0 m/s to 8 m/s.

TEST 3–**Tracking performance test in a specific acceleration and deceleration transition status**: Three experiments were performed. A set of commands in the pitch controller were first carried out to test the flight trim condition. Then, slow, reciprocating yaw channel instructions were implemented to validate the characteristics of latitudinal trim. Finally, a set of pre-defined pulse instructions were executed to test the tracking performance of the longitude and latitude features. In this test, the support mechanism allowed for three-DOF to be released, the throttle of the rotor was set to values of 60%, 80%, and 100% of the hovering speed, respectively, rotor power was set to 0%, 50%, and 100% of the cruise speed, and the incoming flow speed stayed at 10m/s, 15m/s, and 20m/s, respectively.

TEST 4–**Tracking performance test in fixed-wing mode:** The experimental procedures in this test were the same as those in TEST 3. The support mechanism allowed for three-DOF to be released, the throttle of the rotor was set to 0%, 50%, and 100% of the hovering speed, respectively, and the incoming flow speed stayed at 10 m/s, 20m/s 25m/s, and 30m/s.

TEST 5–**Accelerated transition phase simulation test:** The experimental procedures in this test were the same as those in TEST 3. The support mechanism allowed for three-DOF to be released. Depending on the GCS or the receiver, the throttle of the rotor varied, and the incoming flow speed increased from 0 to 25 m/s.

TEST 6–**Deceleration transition phase simulation test:** The experimental procedures in this test were the same as in TEST 3. The support mechanism allowed for three-DOF to be released. Depending on the GCS or the receiver, the throttle of the rotor varied, and the incoming flow speed decreased from 25 to 0 m/s.

FIGURE 25. The outdoor flight test model of the ET120.

TABLE 3. Geometric parameters of ET120.

Geometric parameters	Value
Reference area (m^2)	3.0103
Wing span (m)	5.8
Mean aerodynamic chord (m)	0.6
Mass (k_g)	120
Rotational inertia of the x_b -axis($k_g \cdot m^2$)	80

D. RESULTS OF EXPERIMENTAL FLIGHT TEST

This section presents the results of the outdoor flight test to verify the control frame based on the $\mathcal{L}_1$ adaptive controller. In real-word flight tests, a prototype of the ET120, as shown in FIGURE 25, is employed. And the corresponding geometric parameters are given in Table 3.

The $\mathcal{L}_1$ FCS was tested and verified using Monte Carlo simulations and hardware-in-the-loop simulations before the empirical flight tests. The on-board autopilot had an STM32F765VGT6 216 MHz CPU and a dual redundant automatic heading reference system. The $\mathcal{L}_1$ adaptive controller ran at 200 Hz in hard real-time and used the bilinear discrete method. We simulated the construction of the FCS in MATLAB/SIMULINK and used embedded coder technology to generate C code for direct deployment to the embedded platform. The flight plan was a complex multi-mode process including the vertical take-off, acceleration transition, cruise flight, deceleration transition, and vertical landing. The tracking performance of the $\mathcal{L}_1$ controller having been verified, the mission flight test can be carried out. Before the mission flight, the flight control logic needed to be tested step by step. The flight test procedures were as follows:

Case 1. Vertical take-off and landing test. The ET120 began to take off vertically when set to autonomous mode. When it had climbed to the safety altitude (usually less than five meters), it hovered in the safety window. Then, the vertical landing process was started by the GCS sending an abort-take-off instruction or the receivers' throttle channel being turned down to 25%. Then the vertical descending logic was executed until final touchdown at the landing point. The profile of vertical take-off and landing test is depicted in FIGURE 26.

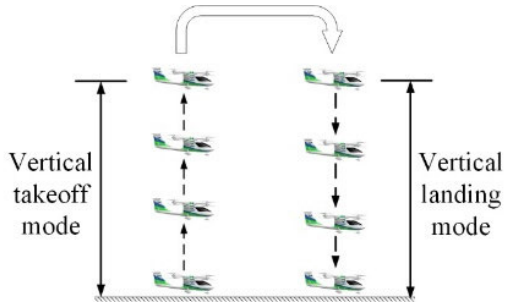

FIGURE 26. Mission profile of vertical take-off and landing modes.

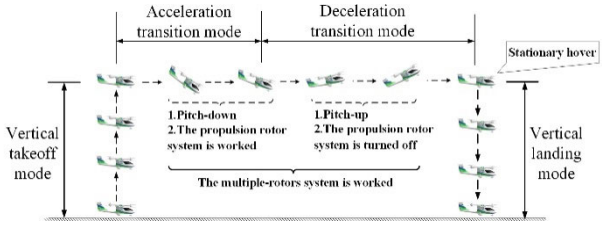

FIGURE 27. Mission profile of acceleration and deceleration transition mode.

Case 2. Acceleration and deceleration test. The content-related tests were divided into low and high acceleration transition tests. The acceleration transition process was activated and the ET120 began to forward accelerate with a pitch-down maneuver once it had vertically climbed to the cruise altitude and aligned its nose to the reference route. In the early stage of acceleration, the process was aborted and ET120 returned to hovering in preparation for vertical descent and touchdown, according to the landing instruction of the GCS or the receiver's throttle channel being turned down to 25% to test the low acceleration transition logic. In the final acceleration transition phase, when ET120 accelerated to close to transition speed, the deceleration transition logic was activated to re-engage it to stationary hover in preparation for landing instructions from the GCS. The profile of the transition flight test is depicted in FIGURE 27.

Case 3. Flight in the entire envelope. The ET120 vehicle started in vertical take-off mode. When it had climbed to the cruise altitude and was aligned with the given route, it switched to the acceleration transition mode. Once its airspeed had reached cruise speed, the vehicle turned to fixed-wing mode and began to level-flight, after which the deceleration and landing processes were re-engaged until it had approached the landing waypoint. At landing point, it completed the entire flight plan by switching to vertical landing mode. The profile of the complete flight plan is depicted in FIGURE 28.

During the flight test, the autopilot continuously transmitted ET120's telemetry data to the ground station at 5 Hz, and the ground station monitored its status in real time. A video showing its flight performance is available at (https://www.youtube.com/watch?v=_DHxItXbzKQ).

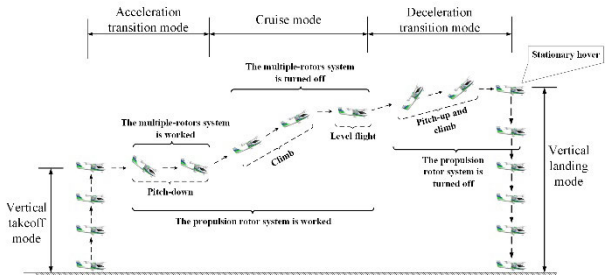

FIGURE 28. Mission profile of the complete flight plan.

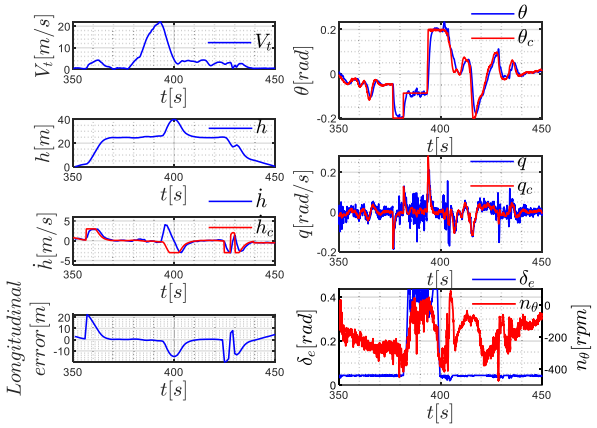

FIGURE 29. Flight data of vertical and longitudinal motions.

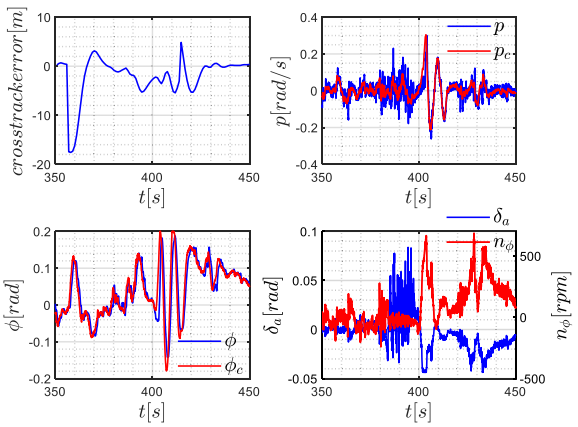

FIGURE 30. Flight data of lateral motion.

1. Flight test of acceleration and deceleration transition phases

Before the complete flight test is performed, the most challenging acceleration and deceleration transition tests are indispensable. The transition speed in the tests was set to 8 m/s at the start and ended at 28 m/s to gradually approach the cruise speed of 30 m/s. FIGURE 29 and FIGURE 30 indicate the corresponding results of the flight test at a transition speed of 22 m/s. The ET120 shared $\mathcal{L}_1$ adaptive augmentation controllers and control allocator both in the acceleration and

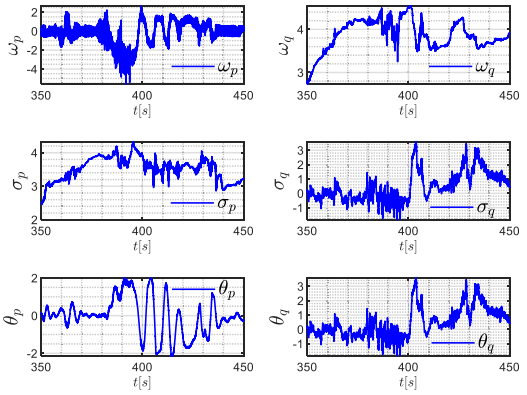

FIGURE 31. Flight data of adaptive estimation factor of the pitch and roll channels. σ_q, ω_q, and θ_q are the estimated adaptive factors of the pitch channel. σ_p, ω_p, and θ_p are the estimated adaptive factors of the roll channel.

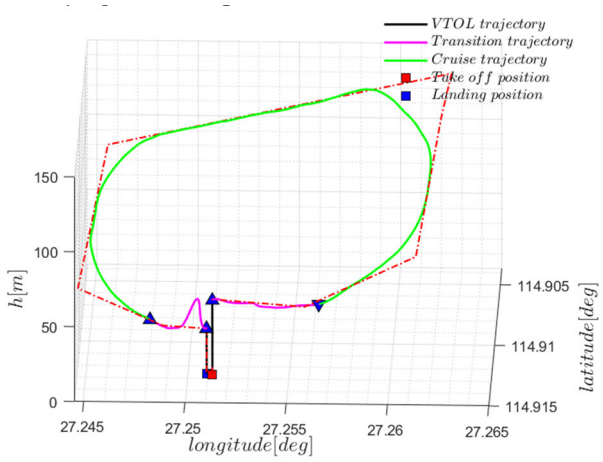

FIGURE 32. Results of the complete flight plan.

the deceleration transition phases. The attitude instructions were obtained through the guidance layer.

As shown in FIGURE 29, in the early acceleration transition phase (begins at t=380s), a -10 degree pitch angle, $\theta_c = -10^\circ$, enabled the ET120 to quickly accelerate, and a rotor speed of 2000 rpm was required to balance gravity. During the acceleration phase, the wing body provided partial balanced lift to mitigate the burden on the power system of the rotor. When the ET120 attained the transition speed, the required rotor speed decreased to 1800 rpm. In the final acceleration transition phase (begins at t=385s), the bow attitude was changed to -5 degrees, $\theta_c = -5^\circ$. This was done for two purposes: to reduce the forward force and to decelerate the drag caused by the frontal area. It took 12.5 s to approach the conversion velocity of 22 m/s and 7.2 s to decelerate the craft to hovering. In the deceleration transition phase (begins at t=392.5s), a 10-degree pitch angle was maintained to produce a braking effect. The deceleration strategy of maintaining the pitch angle considered the flight performance of the fixed wing and the rotor's control capability to make use of its jump maneuver to transform kinetic energy into potential energy quickly. Throughout the transition process, the power system of the rotor operated at a 60% control margin at least to resist external disturbances while the elevator locked into saturation to trim the additional aero-moment caused by it. This is a unique balancing feature of the ET120 in the transition process. FIGURE 29 and FIGURE 30 show that the attitude and the attitude rate loops helped maintain tracking performance in different flight modes (shown by the similarity of the red line and blue line). In the guidance layer, lower bandwidth gains were selected to decouple the inner loop, and the longitudinal and cross-track errors were controlled to within a narrow range. In addition, the flight trimming characteristics in actual flight testing were similar to those in the simulation model established based on the BEMT. The fast BEMT-based calculation model met the demands of the control design and simulation.

FIGURE 31 demonstrates the variations of $\mathcal{L}_1$ adaptive factors $\omega_p(\omega_q)$, $\theta_p(\theta_q)$ and $\sigma_p(\sigma_q)$. The estimates θ_p and θ_q are used to account for errors in the model. The estimates ω_p and ω_q are calculated the uncertainty of the control effectiveness. The estimates σ_p and σ_q are utilized to estimate unmatched uncertainties. The shape of the θ_p and θ_q factors is similar with p and q, showing that $p(q)$ mainly acts as a scaling factor. In the forward acceleration transition flight phase, due to the variations of aerodynamic moments which leads to discrepancy between the real and the reference model, the adaptive factors correspondingly alter variably to maintain the desired closed loop dynamics. And all the adaptive factors are uniformly bounded during the whole transition process.

2. Flight test of the complete flight plan

This subsection presents the complete flight test using the $\mathcal{L}_1$ adaptive augmentation technique, multi-modal control logic, and additional control allocator. The complete reference route of ET120 is depicted in FIGURE 32. The mission profile was consistent with Case 3. The ET120 began take-off in the red square and landed on the gray square to complete its mission. Based on the calculated performance, the cruising speed was constantly maintained at 33 m/s, the roll angle in fixed-wing mode was limited to 0.5 rad, and the climbing rate was limited in the range $[-4, 4]$ m/s. The flight data in FIGURE 33 show that the $\mathcal{L}_1$ adaptive augmentation technique helped maintain satisfactory trajectory tracking performance in the time-varying transition phase.

V. RESULTS

The ET120 is a new member of eVTOLs being explored by COMAC, which is developing products for the commercial market. In the work presented here, the $\mathcal{L}_1$ adaptive augmentation-based FCS and corresponding flight test technology were developed for the large-scale eVTOL platform. By considering the influence of oblique inflow to the rotors in transition flight, we first established a fast rotor dynamics model based on BEMT with asymmetric inflow correction. Then, the SISO $\mathcal{L}_1$ adaptive augmentation controllers were

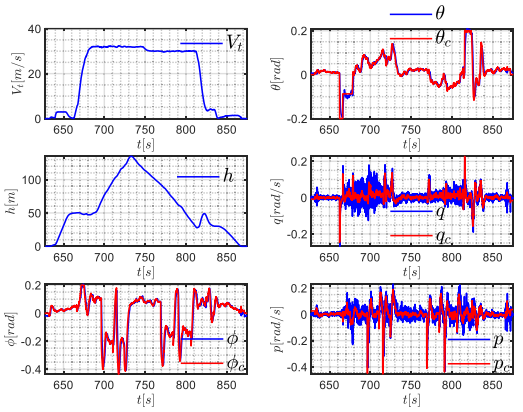

FIGURE 33. Flight data of real word flight test.

designed and theoretically analyzed for the control stabilization. In addition, a practical dynamic inversion type control allocation criterion that relied on the scale of the frequency domain was introduced to overcome the redundant control mechanism. Owing to the complicated flight modules of eVTOLs, we also developed a layered FMS to programmatically operate different flight modes. Finally, the above algorithms were tested in a wide range of specific virtual and empirical flight tests. The results of applying $\mathcal{L}_1$ adaptive augmentation to ET120 reflected enhanced flight capabilities and tracking performance.

Given the results presented above, the following points can be concluded. First, the BEMT can be applied in the modeling of a rigid rotor with no flapping hinge and extended to handle the asymmetric inflow situations, which has a similar result to the CFD methods and a much shorter computing cycle. Second, applying L1 adaptive control theory to the baseline angular rate control of an eVTOL can enhance the flight quality to level 1. Third, the L1 adaptive theory can be applied to new configurations whose aerodynamic characteristics and dynamic characteristics are unfamiliar to aerospace engineers, including the eVTOL held up in this work, and potentially, tilt-rotors and fly-wings. Fourth, a flight control system with multiple layers can be designed with a proper flight management logic to reject the accident in an actual flight test. Finally, the virtual flight test technologies can be applied before an actual flight test experiment to reveal the dynamic characteristics of the close-loop plant in the real world and reduce the uncertain factors in the actual flight tests.

However, the L1 methods lacks some evaluating methods in frequency domain, the performance evaluation in the design phase can only be verified by the amounted Monte Carlo simulations, which is comparatively time-consuming. In future work, we plan to focus on improving the criteria for $\mathcal{L}_1$ adaptive design to solve the trade-off between flight quality and robustness. Some tools of theoretical analysis are also needed for the verification and validation of the $\mathcal{L}_1$-augmented system.

APPENDIX

Definition of L_∞-norm and L_1-norm.

For a signal $\xi\,(t) \in R^n$, L_∞-norm are defined as

$$\|\xi\|_{L_\infty} \triangleq \max_{1\le i\le n}\left\{\sup_{\tau\ge 0}|\xi_i(\tau)|\right\} < \infty$$

where $\xi + i$ is the i-th component of ξ.

And L_1-norm are defined as

$$\|\xi\|_{L_1} \triangleq \int_0^\infty \|\xi(\tau)\|\,d\tau < \infty$$

where $\|(\cdot)\|$ denotes any of the vector norms.

EXTERNAL LINKS

The video of virtual flight test of ET120 is available at (https://www.youtube.com/watch?v=XCRWvHmeiak), and the video of real-word flight tests is available at (https://www.youtube.com/watch?v=_DHxItXbzKQ).

REFERENCES

[1] T. Lombaerts, J. Kaneshige, and M. Feary, "Control concepts for simplified vehicle operations of a quadrotor eVTOL vehicle," in *Proc. AIAA AVIATION FORUM*, Jun. 2020, p. 3189.

[2] M. Daskilewicz, B. German, M. Warren, L. A. Garrow, S.-S. Boddupalli, and T. H. Douthat, "Progress in vertiport placement and estimating aircraft range requirements for eVTOL daily commuting," in *Proc. Aviation Technol., Integr., Oper. Conf.*, Jun. 2018, p. 2884.

[3] B. German, M. Daskilewicz, T. K. Hamilton, and M. M. Warren, "Cargo delivery in by passenger eVTOL aircraft: A case study in the San Francisco bay area," in *Proc. AIAA Aerosp. Sci. Meeting*, Kissimmee, FL, USA, Jan. 2018, p. 2006.

[4] S. S. Chauhan and J. R. R. A. Martins, "Tilt-wing eVTOL takeoff trajectory optimization," *J. Aircraft*, vol. 57, no. 1, pp. 1–20, 2019.

[5] S. Swarnkar, H. Parwana, M. Kothari, and A. Abhishek, "Biplane-quadrotor tail-sitter UAV: Flight dynamics and control," *J. Guid., Control, Dyn.*, vol. 41, no. 5, pp. 1049–1067, May 2018.

[6] Z. Wang, Z. Gong, Y. Chen, M. Sun, and J. Xu, "Practical control implementation of tri-tilt rotor flying wing unmanned aerial vehicles based upon active disturbance rejection control," *Proc. Inst. Mech. Eng., G, J. Aerosp. Eng.* vol. 234, no. 4, pp. 60–943, 2020.

[7] A. J. Calise and R. T. Rysdyk, "Nonlinear adaptive flight control using neural networks," *IEEE Control Syst. Mag.*, vol. 18, no. 6, pp. 14–25, Dec. 1998.

[8] M. Kamel, M. Burri, and R. Siegwart, "Linear vs nonlinear MPC for trajectory tracking applied to rotary wing micro aerial vehicles," *IFAC-PapersOnLine*, vol. 50, pp. 69–3463, Jul. 2017.

[9] Y. Gu, B. Seanor, G. Campa, M. R. Napolitano, L. Rowe, S. Gururajan, and S. Wan, "Design and flight testing evaluation of formation control laws," *IEEE Trans. Control Syst. Technol.*, vol. 14, no. 6, pp. 112–1105, Oct. 2006.

[10] T. Woodbury and J. Valasek, "Synthesis and flight test of automatic landing controller using quantitative feedback theory," *J. Guid. Control Dyn.*, vol. 39, no. 9, pp. 1994–2010, Sep. 2016.

[11] C. Cao and N. Hovakimyan, "Design and analysis of a novel L1 adaptive controller, part I: Control signal and asymptotic stability," in *Proc. Amer. Control Conf.*, Minneapolis, MN, USA, Jun. 2006, pp. 3403–3408.

[12] C. Cao and N. Hovakimyan, "Design and analysis of a novel L1 adaptive controller, part II: Guaranteed transient performance," in *Proc. Amer. Control Conf.*, Minneapolis, MN, USA, Jun. 2006, pp. 3403–3408.

[13] T. Leman, E. Xargay, G. Dullerud, N. Hovakimyan, and T. Wendel, "L1 adaptive control augmentation system for the X-48B aircraft," in *Proc. AIAA Guid., Navigat., Control Conf.*, Chicago, IL, USA, Aug. 2009.

[14] E. Xargay, N. Hovakimyan, V. Dobrokhodov, R. Statnikov, I. Kaminer, C. Cao, and I. Gregory, "L1 adaptive flight control system: Systematic design and verification and validation of control metrics," in *Proc. AIAA Guid., Navigat., Control Conf.*, Toronto, ON, Canada, Aug. 2010, p. 7773.

[15] R. Beard, C. Cao, and N. Hovakimyan, "An L1 adaptive pitch controller for miniature air vehicles," in *Proc. AIAA Guid., Navigat., Control Conf. Exhib.*, Keystone, CO, USA, Aug. 2006, p. 6777.
[16] J. Chang, J. Zhu, R. Liu, and W. Dong, "Lateral control for ultra-low altitude airdrop based on the L1 adaptive control augmentation," *Int. J. Control Automat. Syst.*, vol. 16, no. 2, pp. 77–461, 2018.
[17] L. Guo, M. Zhu, B. Nie, P. Kong, and C. Zhong, "Initial virtual flight test for a dynamically similar aircraft model with control augmentation system," *Chin. J. Aeronaut.*, vol. 30, no. 2, pp. 10–602, 2017.
[18] F. Liu, L. Wang, and X. Tan, "Digital virtual flight testing and evaluation method for flight characteristics airworthiness compliance of civil aircraft based on HQRM," *Chin. J. Aeronaut.*, vol. 28, no. 1, pp. 20–112, 2015.
[19] N. Nigam, S. Bieniawski, I. Kroo, and J. Vian, "Control of multiple UAVs for persistent surveillance: Algorithm and flight test results," *IEEE Trans. Control Syst. Technol.*, vol. 20, no. 5, pp. 51–1236, Oct. 2012.
[20] S. Chang, A. Cho, S. Choi, Y. Kang, Y. Kim, and M. Kim, "Flight testing full conversion of a 40-kg-class tilt-duct unmanned aerial vehicle," *Aerosp. Sci. Technol.*, vol. 112, pp. 84–169, May 2021.
[21] L. Yi, S. Zhang, Z. Zhang, X. Zhang, T. Peng, and F. U. Shan, "Multiple hierarchy risk assessment with hybrid model for safety enhancing of unmanned subscale BWB demonstrator flight test," *Chin. J. Aeronaut.*, vol. 32, no. 12, pp. 26–2612, 2019.
[22] S. Saderla, Y. Kim, and A. K. Ghosh, "Online system identification of mini cropped delta UAVs using flight test methods," *J. Aerosp. Sci. Technol.* vol. 80, pp. 53–337, Sep. 2018.
[23] J. G. L. *Principles of Helicopter Aerodynamics*. Cambridge, U.K.: Cambridge Univ. Press, 2006, pp. 92–97.
[24] J. Harris and J. Valasek, "Direct L1-adaptive nonlinear dynamic inversion control for command augmentation systems," in *Proc. AIAA Guid., Navigat., Control Conf.*, Kissimmee, FL, USA, Jan. 2018, p. 1575.
[25] N. Hovakimyan and C. Cao, "L1 adaptive control theory—Guaranteed robustness with fast adaptation," in *Advances in Design and Control*, no. 21. Philadelphia, PA, USA: SIAM, 2010.
[26] I. Kaminer, A. Pascoal, E. Xargay, N. Hovakimyan, C. Cao, and V. Dobrokhodov, "Path following for small unmanned aerial vehicles using L1 adaptive augmentation of commercial autopilots," *J. Guid., Control, Dyn.*, vol. 33, no. 2, pp. 550–564, Mar. 2010.
[27] J.-B. Pomet and L. Praly, "Adaptive nonlinear regulation: Estimation from the Lyapunov equation," *IEEE Trans. Autom. Control*, vol. 37, no. 6, pp. 729–740, Jun. 1992.
[28] K. Bordignon and J. Bessolo, "Control allocation for the X-35b," in *Proc. Biennial Int. Powered Lift Conf. Exhib.*, Williamsburg, VA, USA, Nov. 2002, pp. 130–150.
[29] W. Durham, K. A. Bordignon, and R. Beck, *Aircraft Control Allocation*. Chichester, U.K.: Wiley, 2017.

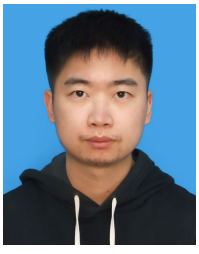

ZIAN WANG was born in Taizhou, Zhejiang, China, in March 1994. He is currently pursuing the Ph.D. degree in aeronautical engineering with the Nanjing University of Aeronautics and Astronautics, Nanjing, China. He held three search positions at Shenyang Aircraft Design and Research Institute, in 2016, the China Academy of Space Technology, in 2018, and Commercial Aircraft Corporation of China Ltd., in 2020. His research interests include advanced STOVL and eVTOL aircrafts, advanced missile systems, reusable launch vehicle, flight dynamics modeling and analysis, motion planning, guidance law, adaptive control, active disturbance rejection control, model predictive control, cooperative and formation control, and flight-testing.

ZHENG GONG received the Ph.D. degree in aeronautical engineering from the Nanjing University of Aeronautics and Astronautics, Nanjing, China. He was a Visiting Scholar with the University of Bristol, U.K., in 2014. He is currently a Lecturer with the College of Aerospace Engineering, Nanjing University of Aeronautics and Astronautics. He leads the Flight Dynamics Group, Nanjing University of Aeronautics and Astronautics. His research interests include advanced aircraft systems, advanced missile systems, flight dynamics modeling and analysis, flying qualities evaluation, flight parameter identification, forces combat efficiency, trajectory optimization, flight control system design, and simulations and flight-testing.

CHI ZHANG received the B.Eng. degree in electromechanical engineering from the University of Southampton, U.K., the M.Sc. degree in aerospace vehicle design from Cranfield University, U.K., and the M.Eng. degree. He is currently pursuing the Doctor of Engineering degree in system engineering with Tsinghua University. He is also qualified as a C.Eng. and PPL. He is the Project Lead Engineer with the Beijing Aeronautical Technology Research Institute (BATRI) of COMAC.

JUN HE is currently a Master, a Senior Experimenter, and a Lecturer with the Shenyang University of Aeronautics and Astronautics, the Vice Director of the College of Aeronautics and Astronautics, Institute of Space Vehicle Dynamics and Control, the Leading Talent of Senior Talents in Shenyang City, the Executive Deputy Director of the Technical Working Committee of the China International Aircraft Design Platoon Competition of the State Administration of Sports, and the General Manager of Zhuhai Tianqing Aerospace Technology Company Ltd., and is good at the overall design, manufacturing, testing and flight test of composite aircraft and its components. He is also the Former Vice President of the Liaoning General Aviation Research Institute, the General Manager of Liaoning Ruixiang General Aircraft Manufacturing Company Ltd. and the Project Technical Leader of RX1E (Ruiyong), the first electric two-seat light aircraft in China.

SHENGCHEN MAO was born in Taizhou, Jiangsu, China, in March 1998. He is currently pursuing the master's degree majoring in aeronautical and astronautical engineering with the College of Aerospace Engineering, Nanjing University of Aeronautics and Astronautics. His research interests include flight dynamics modeling and analysis, flight control system design, and adaptive control and guidance for advanced STOVL and eVTOL aircrafts.